1 Retrieval of aerosol properties from zenith sky radiance measurements

2 Sara Herrero-Anta[1], Roberto Román[1], David Mateos[1], Ramiro González[1], Juan Carlos
3 Antuña-Sánchez[2], Marcos Herreras-Giralda[2], Antonio Fernando Almansa[3,4], Daniel
4 González-Fernández[1], Celia Herrero del Barrio[1], Carlos Toledano[1], Victoria E. Cachorro[1]
5 and Ángel M. de Frutos[1].

6 [1]Group of Atmospheric Optics, University of Valladolid, Paseo de Belén 7, 47011 Valladolid, Spain.
7 [2]GRASP SAS, Remote Sensing Developments, Villeneuve D'Ascq, France
8 [3]Izaña Atmospheric Research Center (IARC), State Meteorological Agency of Spain (AEMET), 38001
9 Santa Cruz de Tenerife, Spain.
10 [4]Cimel Electronique, 75011 Paris, France.

11 *Correspondence to*: Sara Herrero-Anta (sara@goa.uva.es)

12 **Abstract.** This study explores the potential to retrieve aerosol properties with the GRASP algorithm
13 (Generalized Retrieval of Atmosphere and Surface Properties) using as input measurements of zenith sky
14 radiance (ZSR), which are sky radiances measured in the zenith direction, recorded at four wavelengths by
15 a ZEN-R52 radiometer. To this end, the ZSR measured at 440, 500, 675 and 870 nm by a ZEN-R52
16 (ZSR_{ZEN}), installed in Valladolid (Spain), is employed. This instrument is calibrated intercomparing the
17 signal of each channel with coincident ZSR values simulated (ZSR_{SIM}) at the same wavelengths with a
18 radiative transfer model (RTM). These simulations are carried out using the GRASP forward module as
19 RTM and the aerosol information from a collocated CE318 photometer belonging to the AERONET
20 network (Aerosol and Robotic Network) as input. Dark signal and the signal dependence on temperature
21 are characterized and included in the calibration process. The uncertainties on each channel are quantified
22 by an intercomparison with a collocated CE318 photometer, obtaining lower values for shorter
23 wavelengths; between 3% for 440 nm and 21% for 870 nm. The proposed inversion strategy for the aerosol
24 retrieval using the ZSR_{ZEN} measurements as input, so-called GRASP-ZEN, assumes the aerosol as an
25 external mixture of five pre calculated aerosol types. A sensitivity analysis is conducted using synthetic
26 ZSR_{ZEN} measurements, pointing out that these measurements are sensitive to aerosol load and type. It also
27 assesses that the retrieved aerosol optical depth (AOD) values in general overestimates the reference ones
28 by 0.03, 0.02, 0.02 and 0.01 for 440, 500, 675, 870 nm, respectively. The calibrated ZSR_{ZEN} measurements,
29 recorded during two and half years at Valladolid, are inverted by GRASP-ZEN strategy to retrieve some
30 aerosol properties like AOD. The retrieved AOD shows a high correlation with respect independent values
31 obtained from the collocated AERONET CE318 photometer, with a determination coefficient (r^2) about
32 0.86, 0.85, 0.79 and 0.72 for 440, 500, 675 and 870 nm, respectively, and finding uncertainties between
33 0.02 and 0.03 with respect to the AERONET values. Finally, it is studied the goodness of other retrieved
34 aerosol properties like aerosol volume concentration for total, fine and coarse modes.

35 **Keywords:** zenith sky radiance, ZEN, GRASP, aerosol optical depth, AERONET, photometer

36 1. Introduction

37   Atmospheric aerosols constitute the biggest source of uncertainty in the assessment of Climate Change
38 as assessed by Myhre et al., (2013), and yet, one decade later, not significant improvements have been made
39 on this respect (Cissé et al., 2022). This is largely due to their high spatial and temporal variability across
40 the globe and the complexity of its interaction with clouds (aerosol-cloud interactions) and solar radiation
41 (aerosol-radiation interactions) (Boucher et al., 2013).
42   For a better understanding of aerosols and their behaviour and interactions, it is needed a high spatial
43 and temporal monitoring coverage. Satellite measurements provides, in general, a high spatial resolution
44 covering the whole Earth but with a low time resolution. On the other hand, some global ground-based
45 networks, like AERONET (AErosol RObotic NETwork; Holben et al., 1998), were established to monitor
46 aerosols around the globe. In the case of AERONET, this network counts with hundreds of stations
47 distributed worldwide and imposes standardization of instruments, calibration, processing and distribution.
48 The standard instrument of AERONET is CE318 photometer (Cimel Electronique SAS), which records
49 measurements of sun (and also lunar in recent models) irradiance and sky radiance in several wavelengths.
50 Aerosol optical depth (AOD) can be derived using the measurements of sun (or lunar if available) such as

51 in the case of AERONET, applying the Beer-Lambert-Bouguer law on the instrument's output voltage as
52 described in Holben et al. (1998)and Giles et al. (2019). AERONET also retrieves more complex aerosol
53 properties, like aerosol size distribution and refractive indices, using an inversion algorithm that uses as
54 input sky radiances at different angles and wavelengths, together with the AOD values (Sinyuk et al., 2020).
55   Another inversion algorithm is the GRASP code (Generalized Retrieval of Atmosphere and Surface
56 Properties; www.grasp-open.com), which is a free and open-source code that allows a flexible retrieval of
57 aerosol properties using measurements taken from many different instruments and a combination of them
58 (Dubovik et al., 2014; 2021). The continuous development and versatility of the code allows to explore new
59 alternatives to apply the code to different instruments. In this sense, some authors used GRASP to retrieve
60 aerosol properties using as input measurements, among others, of: satellites (Chen et al., 2020; Wei et al.,
61 2021); nephelometers (Espinosa et al., 2017); multi-wavelength AOD (Torres et al., 2017); AOD and sky
62 radiance from photometers with signal from lidars (Lopatin et al., 2013; Benavent-Oltra et al., 2017; Tsekeri
63 et al., 2017; Molero et al., 2020) or ceilometers (Román et al., 2018; Titos et al., 2019; Herreras et al.,
64 2019); stand-alone all-sky cameras (Román et al., 2022) and their combination with lunar photometers
65 (Román et al., 2017) and lidar (Benavent-Oltra et al., 2019).
66   A new instrument that could be used for GRASP retrievals is the ZEN-R52 (Sieltec Canarias S.L.),
67 which has already been used to retrieve AOD values by other methods (Almansa et al., 2020). The ZEN-
68 R52 measures the zenith sky radiances (ZSR) at five different wavelengths every minute, giving continuous
69 ZSR values during daytime at 440, 500, 675, 870 and 940 nm (this latter channel is dedicated to the study
70 of water vapour). As advantage, this instrument has not moving parts and, in general, is cheaper than more
71 complex photometers, which allows the installation of more instruments obtaining a higher spatial
72 coverage. Almansa et al., (2020) presented the ZEN-R52 and developed a method to retrieve AOD values
73 from ZSR using a lookup table (LUT) created for the site of study, Izaña (Canary Island, Spain), considering
74 uniquely dust aerosol, which is the main aerosol type in the area due to the proximity to the Saharan desert.
75   In this framework, the main objective of this work is to develop a new methodology to retrieve AOD
76 and other aerosol properties with GRASP using calibrated ZSR at 440, 500, 675 and 870 nm from a ZEN-
77 R52 instrument. This retrieval strategy is not linked to the place of study and therefore it allows to distribute
78 the instrument worldwide, avoiding the need to create a different LUT for each site. In addition, we propose
79 an in-situ method for the calibration of the ZEN-R52.
80   The following paper is structured as follows: Section 2 gathers information regarding the
81 instrumentation and retrieval methods employed, as well as the study location. The procedure and results
82 of the calibration of the ZSR at the four wavelengths used is explained in Section 3, while Section 4 is used
83 to evaluate and drive a sensitivity study of the algorithm employed for the retrieval of aerosol properties.
84 Finally, results obtained using the proposed methodology for the retrieval of aerosol properties are shown
85 in Section 5, and Section 6 summarizes the main conclusions of the study.

2. Data and method

2.1 Site and instrumentation

2.1.1 Valladolid GOA-UVa station

90 The place of study is located in Valladolid (Spain), a medium-sized city with a population of about 400000
91 inhabitants including the metropolitan area. The city's climate is Mediterranean (Csb Köppen–Geiger
92 climate classification). It presents predominantly 'clean continental' aerosol with frequent episodes of
93 Saharan desert dust intrusions, especially in summer, when the highest AOD monthly mean values are
94 reached (Bennouna et al., 2013; Román et al., 2014; Cachorro et al., 2016).
95   The Group of Atmospheric Optics of the University of Valladolid (GOA-UVa) manages an
96 instrumentation platform installed on the rooftop of the Science Faculty (41.6636° N, 4.7058° W; 705 m
97 asl), where diverse remote sensing instruments continuously run providing complementary information
98 about radiance, clouds, water vapour, trace gases and aerosols. Two instruments from this station are used
99 in this work: the CE318 photometer and the ZEN-R52 radiometer. The corresponding calculations and
100 additional information will be referred and obtained for this location.

2.1.2 CE318 photometers and AERONET products

102   Since 2006 the GOA-UVa has been one of the calibration facilities in charge of the calibration of
103 AERONET standard instruments and is currently part of the European infrastructure ACTRIS (Aerosol,

104   Clouds and Trace Gases Research Infrastructure). The group is also actively contributing to the solar and
105   moon photometry research (Barreto et al., 2019; González et al., 2020; Román et al., 2020). Due to
106   calibration purposes, the GOA-UVa has almost always two reference AERONET photometers (masters)
107   continuously operating on its rooftop platform for the calibration of the field instruments by
108   intercomparison with these masters. The CE318 measures direct sun (and lunar for the recent model CE318-
109   T; Barreto et al., 2016) irradiance at several narrow spectral bands by means of a rotating filters wheel.
110   These direct measurements are used to derive the AOD (Giles et al., 2019) for all the available filters with
111   and uncertainty of ±0.01 for wavelengths longer than 440 nm and ±0.02 for the UV (Holben et al., 1998).
112   Sky radiances at several wavelengths are also measured by the CE318 on different scanning scenarios, and
113   these sky radiances are combined with AOD values in the AERONET inversion algorithm to obtain
114   microphysical and optical aerosol properties like aerosol volume size distribution and complex refractive
115   index (Sinyuk et al., 2020). The sky radiances are calibrated against a calibrated integrating sphere
116   following AERONET standards, obtaining an uncertainty of 5% for those measurements (Holben et al.,
117   1998).
118   In this work, we use AOD, sky radiance values and retrieved aerosol products from inversions from
119   AERONET version 3 level 1.5. These data have been directly downloaded from the AERONET webpage
120   (https://aeronet.gsfc.nasa.gov), which include near-real-time automatic cloud-screening and quality control
121   filters (level 1.5). The inversion products with a sky error above 10% have been rejected in this study to
122   warranty the quality of the retrievals.

2.1.3   ZEN-R52

124   The main instrument used in this work is the ZEN-R52 radiometer, installed in the GOA-UVa
125   platform since April 2019. Since that moment the ZEN-R52 has been continuously operating in Valladolid,
126   except for some short malfunction periods caused by technical issues. This study uses the recorded data
127   from April 2019 until September 2021. The device was jointly developed by Sieltec Canarias S.L. and the
128   Izaña Atmospheric Research Center (IARC) to monitor AOD from sky radiance measurements at the zenith
129   direction and at different spectral bands (Almansa et al., 2017; 2020). The instrument has five filters with
130   nominal wavelengths centred at 440, 500, 675, 870 and 940 nm with a bandwidth of 10 nm and an estimated
131   precision of ±2 nm in the central wavelength. Each filter is over a silicon diode (350–1050 nm) with a 16-
132   bit resolution, over a high dynamic acquisition range. The 940 nm filter was recently included in this new
133   version for precipitable water vapour retrieval but this channel is not used in this work since it is focused
134   on aerosols. The ZEN-R52 optical configuration achieves a field of view smaller than 2º. It is equipped
135   with a small aluminium weatherproof and protected by a thick borosilicate BK7 window, with no moving
136   parts. All of this is mounted in such a way that the collimated sky radiance in the direction of the zenith
137   reaches to the sensors. The instrument results to be very robust and can operate in a wide temperature range,
138   between −40º and 85ºC. A more detailed technical description of the instrument can be found in Almansa
139   et al. (2017; 2020).
140   The zenith sky radiance measurements at all channels are made simultaneously, providing an
141   output signal in analogic-to-digital units (ADU) every minute. This output is the computed average of 30
142   samples taken within the minute, providing also an error (ZEN error) associated to the measurement which
143   is the standard deviation of the 30 samples.

2.2 GRASP methodology

145   GRASP contains mainly two independent modules: the 'forward model' and the 'numerical
146   inversion'. The first one is a radiative transfer model (RTM) used to simulate atmospheric remote sensing
147   observations for a characterized atmosphere. The second module, based on the multi-term least squares
148   method (Dubovik and King, 2000), is used in combination with the RTM for a statistically optimized fitting
149   of the observations to retrieve aerosol properties from radiometric measurements (Dubovik et al., 2014).
150   This provides the algorithm with high flexibility since different constrains can be applied to the retrieval
151   and can be modified in order to adapt the retrieval to each specific situation. It is important to mention that
152   GRASP works with normalized radiances (I_{GRASP}), which are related with the measured radiances as:

$$I_{GRASP} = I_{meas} * \pi / E_0 \qquad (1)$$

154   Where I_{meas} is the radiance measured by the instrument and E_0 is the extraterrestrial solar
155   irradiance, both expressed in the same units. The standard ASTM-E490 solar spectrum has been used in
156   this work for the normalization of Eq. (1). This spectrum was calculated for moderate solar activity and

157 medium Sun-Earth distance; therefore, it has been corrected from Sun-Earth distance for each day of the
158 year.

159   2.2.1. Forward module

160   The GRASP forward module is a RTM based on the Succesive Orders or Scattering approach
161 (Lenoble et al., 2007; Herreras-Giralda et al., 2022) which requires information about aerosol, gas, site
162 coordinates and date-time together with the solar zenith angle (SZA) to characterize the atmosphere
163 scenario. In this study gases and aerosol information are extracted from AERONET direct and inversion
164 products available at Valladolid station. For the gases it has been used the gases optical depth (GOD), while
165 the used aerosol information has been size distribution (in 22 log spaced bins of radius), sphere fraction and
166 complex refractive indices at 440, 675 and 870 nm. Complex refractive index at 500 nm has been
167 interpolated from the values at 440 and 675 nm. The bidirectional reflectance distribution function (BRDF)
168 data is also used as input in GRASP. The used BRDF values are extracted from an 8-day climatology
169 created for the place of study using satellite data; specifically, the MCD43C1 product from MODIS V005
170 collection (Schaaf et al., 2011) for the 2000–2014 period (see Román et al. 2018 for more details about
171 these climatology values).

172   The ZSR has been simulated at 440, 500, 675 and 870 nm with the GRASP forward module using
173 all the mentioned input data whenever it was available. These simulations have been used for calibration
174 purposes as can be observed in Section 3, but also for the sensitivity analysis with synthetic data of Section
175 4.2. ZSR simulations are also performed for Section 4.1, but in this case the aerosol properties have been
176 obtained for precalculated aerosol types instead of real data from AERONET.

177   2.2.2 Inversion strategy

178   The present study aims to retrieve aerosol properties with GRASP using as input the calibrated
179 ZSR from the ZEN-R52 at four effective wavelengths. The versatility of GRASP allows different
180 approaches to model aerosols to maximize the possibilities of the different retrieval schemes. Due to the
181 reduced amount of information produced by the ZEN-R52, the approach called 'models' has been chosen
182 (Chen et al., 2020). This is a simple and fast processing approach where aerosol is assumed to be an external
183 mixture of several aerosol models. In this case the approach assumes five aerosol types which correspond
184 to the typical aerosols on Earth: smoke, urban, oceanic, dust and urban polluted. Each model has a fixed
185 particle size distribution, refractive indices and sphere fraction, containing the already pre-calculated phase
186 matrix, and the extinction and absorption cross-sections (see Fig. S1 for a representation of the size
187 distribution of each model).
188 This way, the inversion strategy retrieves only five independent parameters: the total aerosol volume
189 concentration and the fraction of four models in the mixture (the fifth fraction equals one minus the rest of
190 the fractions). All these retrieved parameters allow to obtain other complex aerosol properties, like size
191 distribution parameters, weighting the individual properties of each model, which are known, by their
192 fraction of the mixture. The size distribution parameters that can be obtained are volume median radius of
193 fine (RF) and coarse (RC) modes, standard deviation of lognormal distribution for fine (σF) and coarse
194 (σC) modes, and aerosol volume concentration for fine (VCF) and coarse (VCC) modes and the total value
195 (VCT). AOD can be also calculated and it is given for each wavelength directly in the GRASP output. Each
196 output, one per retrieval, provides the relative residual differences between the measured ZSR (input) and
197 the ones generated after the inversion (simulated by GRASP forward module under the retrieved scenario)
198 for each wavelength. This residual information will be used to evaluate the goodness of the retrievals,
199 rejecting the non-convergent ones.
200   This proposed strategy requires as input: the calibrated ZSR at four wavelengths, the coordinates
201 of the site, date, time, SZA, the BRDF values obtained from the climatology mentioned above, and the
202 GOD at each wavelength to account for gases effect. The GOD used in this work is obtained from a monthly
203 GOD climatology, which has been created using GOD data retrieved from AERONET for the 2012-2021
204 period in Valladolid. This proposed inversion strategy to retrieve aerosol properties with GRASP using
205 ZEN-R52 measurements has been named as 'GRASP-ZEN'.

206

207   3. Calibration

208   A methodology for the ZEN-R52 calibration is proposed in this Section. This methodology is a field
209   campaign which does not require laboratory measurements except for the dark signal characterization, and
210   it is based on four steps: dark signal correction, quality data filtering, temperature correction, and a final
211   comparison against simulated values to convert the output signal from ADU into radiance units (Wm^{-2}nm^{-1}sr^{-1}). With this purpose ZSR simulations have been performed for the whole dataset of ZEN-R52
212   measurements, using the GRASP forward module fed with the closest AERONET information (Section
213   2.2.1) whenever it was available within ±5 minutes from the ZEN-R52 measurement; considering in good
214   approximation, and as checked later, that aerosol conditions will not change significantly within 5 minutes.
215   Only those AERONET retrievals with a sky error lower than 5% have been used to ensure the quality of
216   the simulations, obtaining a total of 4725 data pairs.
217

219   3.1. Dark signal correction

220   For the dark signal (DS) evaluation, the instrument was fully covered with a black piece and
221   introduced into a thermal chamber in the GOA-UVa facilities. The instrument was subjected to a
222   temperature variation in the range from -10 to 50 °C in darkness conditions. The dark signal registered by
223   each channel at each temperature is shown in Figure 1. It shows a constant behaviour for 440 and 500 nm
224   filters. Contrary, for the other wavelengths a stepped exponential behaviour can be seen. In order to
225   characterize this behaviour, the logarithm of the ZEN dark signal has been fitted to a three-degree
226   polynomial. This fitting is after rounded up to the unit to obtain a stepped fitting. The modelled dark signal
227   is also represented in Figure 1 by the black lines. This modelling has been used to subtract the corresponding
228   dark signal value to the raw signal, obtaining dark signal corrected ZSR (ZSR$_{DSC}$). The DS signal has been
229   characterized in the laboratory in this work in order to cover a high range of temperatures, but it could be
230   calculated from the night-time measurements (dark sky) when a thermal chamber is no available.

231   3.2 Quality control filtering criteria

232   With the dark signal corrected, we compare the field measurements of ZSR$_{DSC}$ against the ZSR
233   simulated values (ZSR$_{SIM}$). This comparison is shown in Figure 2. The points colour in the scatter plots of
234   Figure 2 represent the density of points per pixel as defined by Eilers and Goeman (2004), using a λ=50 for
235   smoothness; all the density scatter plots of this paper were done with the same configuration. The
236   determination coefficient (r^2) is also added in the panels of Figure 2, showing in general good agreement
237   for each channel between ZSR$_{DSC}$ and ZSR$_{SIM}$ but with some outliers regarding the linear trend (see left
238   panels a, c, e and g). These outliers present higher ZSR$_{DSC}$ values than expected and they could be caused
239   by the presence of clouds in the zenith, instrument malfunction and others.

240   To identify and reject the cloud-contaminated or wrong measurements, several parameters have
241   been considered in this subsection: SZA, ZEN error, temperature, and the time interval between the
242   inversion used to simulate the ZSR$_{SIM}$ and the corresponding ZSR$_{DSC}$. Some thresholds have been identified
243   after the visual analysis of these parameters in the scatter plot. For the SZA, the signal of ZEN instrument
244   is higher than the expected for SZA values below 30°, which could be explained by some stray sun light
245   coming to the sensors due to the high elevation of the Sun. Then, ZSR$_{DSC}$ values recorded under SZA below
246   30° have been discarded, but also the values with SZA above 80° due to the low signal registered for this
247   SZAs (See Figure S2 for a clear overview). The ZEN error parameter (Section 2.1.3) can be assumed as a
248   cloud presence indicator, since measurements affected by clouds should register a high ZEN error due to
249   the high variability of the sky radiances during the 1-min measurement. An evaluation of Figure 2 but with
250   points classified by its ZEN error at 440 nm led us to establish a threshold of 4% for the ZEN error in the
251   four channels (See Figure S3). If the measurement of any channel has a ZEN error above this threshold,
252   then the measurements of the four channels are rejected.

253   No clear dependence of the outliers on the rest of the parameters has been observed. The results
254   after applying the mentioned filters (30° < SZA < 80°; ZEN error < 4%) are represented in the right panels
255   (b, d, f and h) of Figure 2. The number of coincident measurements is reduced to 4369 points after applying
256   the quality control but a significant improvement in the determination coefficients is observed, rising from
257   0.96 to 0.99 for the 440nm channel and from 0.80 to 0.95 in the case of 870nm. From now on, all the
258   ZSR$_{DCS}$ measurements used will be assumed to satisfy this quality control unless specified.

259   3.3 Temperature correction

260   In order to check the dependence with temperature of each filter the ratio ZSR_{DSC}/ZSR_{SIM}
261 normalized by the mean ratio is plotted against the temperature in Figure 3. In the left panels (a, c, e and g)
262 of Figure 3 all data points are represented together with the linear fit, showing a constant behaviour for 440
263 and 500 nm, but a clear trend for 675 and 870 nm channels. In order to despise outliners, the ratios were
264 grouped by 2°C bins and its median was calculated whenever the group had at least 40 points. These median
265 values are plotted against the mean temperature of the group's temperatures in Figure 3 right panels (b, d,
266 f and h). The corresponding linear fit coefficients obtained in Figures 3f and 3h has been established to be
267 used to correct the ZSR_{DSC} at 675 and 870 nm applying the next Equation 2:

268 $$ZSR_{TC}(\lambda) = \frac{y_{20(\lambda)}}{a(\lambda)+b(\lambda)T} ZSR_{DSC}(\lambda); \ \lambda = 675, 870 \text{nm} \qquad (2)$$

269   where ZSR_{DSC} is the ZEN signal after dark signal correction and ZSR_{TC} is this signal with the
270 temperature correction; a and b represent the intercept and slope of the final linear fits, respectively; y_{20} is
271 the correspondent y-axis value of the linear fit at the temperature T of 20° C (arbitrary value chosen to
272 normalize). This temperature correction is only applied to the λ-wavelengths of 675 and 870 nm.

273   3.4. Calibration coefficients

274   Once the dark signal correction, quality filtering and temperature correction are applied to the
275 ZEN-R52 raw signal, the definitive comparison between the ZSR from the ZEN-R52 and the ZSR values
276 simulated by GRASP forward module can be done to obtain the calibration coefficients. The density scatter
277 plots between ZSR_{SIM} values and ZSR_{TC} are shown in Figure 4. The slope of the linear fit directly represents
278 the calibration coefficients obtained to transform the ZSR_{TC} signal into radiance units ($Wm^{-2}nm^{-1}sr^{-1}$) for
279 each channel. This calibrated radiance is named ZSR_{ZEN} hereafter.

280   The obtained calibration coefficients and the ones obtained by intercomparison with a calibrated
281 integrating sphere at IARC facilities are shown in Table 1. Table 1 also presents the relative differences
282 between both calibration coefficients using the coefficients from IARC as reference; the uncertainty
283 involved in the latter calibration method procedure is estimated to be 5% by Walker et al. (1991) These
284 differences are 1.39%, -6.54%, -6.72% and -5.89% for 440, 500, 675 and 870 nm, respectively. The
285 proposed calibration method uses the standard ASTM-E490 solar spectrum for transforming the unitless
286 output from GRASP, as indicated in Equation 1. This fact can increase the relative differences between the
287 two calibration methods. However, the calibration method employed here allows to use the same
288 normalization factor that lately will be applied to the ZSR_{ZEN} measurements that will be introduced in the
289 GRASP inversion module, avoiding to introduce a systematic error due to the normalization required by
290 the algorithm. It means that this calibration method is better suited when using the ZSR_{ZEN} values as input
291 for GRASP to retrieve aerosol properties, since there is no need for extraterrestrial spectrum normalization.
292 From now on ZSR_{ZEN} will stand for the calibrated zenith sky radiances measured by the ZEN-R52 satisfying
293 the stablished quality controls (30° < SZA < 80°; ZEN error < 4%).

294   3.5. ZEN-R52 vs. CE318 photometer comparison

295   In order to check the goodness of the calibrated ZEN-R52 measurements, the ZSR_{ZEN} observations
296 have been compared with measurements recorded by collocated CE318 instruments for the hole available
297 dataset of ZEN-R52 measurements. For the comparison, independent measurements from CE318
298 photometers for two different scenarios are employed: the cloud mode (CM) and the principal plane
299 scanning (PPL).

300   3.5.1. Cloud Mode

301   The CE318 sun-sky photometer allows to perform measurements in the 'cloud mode' scenario. It
302 is carried out when the direct sun measurement indicates an obscured sun, and therefore the aerosol retrieval
303 is not possible. This scenario orientates the sensor head into the zenith direction and takes zenith radiance
304 measurements at 9 s intervals for each wavelength, which are obtained by successively rotating an
305 interference filter in front of the detector. The 'cloud mode' scenario was originally implemented to obtain,
306 during this idle time, cloud optical depth from zenith sky radiances at the spectral wavelengths employed
307 by the sun-sky photometer (Chiu et al., 2010) as suggested by Marshak et al., (2000) and Barker and
308 Marshak, (2001).

309   The zenith sky radiances measured under the cloud mode (ZSR_{CM}) have been directly downloaded
310   from the AERONET network webpage. For the comparison with ZEN-R52, quasi-coincident (the closest
311   within ± 1 min) ZSR_{ZEN} and ZSR_{CM} measurements have been obtained and plotted in Figure 5, showing a
312   good correlation between both datasets. The deviation between them is high, likely due to the short-time
313   variation in the cloud radiative field. Figure 5 includes all the ZSR_{ZEN} measurements; the filtering to SZA
314   values and ZEN errors is not applied, since the cloud mode measurements is under cloud presence. In this
315   case, there is not dependence on SZA; outliers do not appear for SZA<30° values. Hence, the ZSR_{ZEN} values
316   are only wrong for SZA<30° when the sun is cloud-free, which confirms the suggested explanation that
317   ZSR_{ZEN} measurements are contaminated by stray sun light under cloud-free conditions when the sun
318   elevation is high (SZA<30°). In addition, it was checked that 86% of the ZEN-52 measurements used in
319   this comparison (which are known to be affected by clouds), present a ZEN error > 4% at least for one
320   channel. This also validates the proposed use of the ZEN error as a rough 'cloud screening'.

321   3.5.2. Principal plane scan

322   CE318 sun-sky photometers allow to perform three different scanning scenarios for sky radiance
323   measurements. One of these scanning scenarios is in the principal plane (PPL) geometry, where the azimuth
324   angle is equal to the solar azimuth angle while the zenith angle varies measuring sky radiances at the same
325   fixed angles regards the SZA. This is done sequentially once for each channel starting at 870nm, followed
326   by 675, 500 and 440 nm channels for each PPL scenario. The PPL geometry allows to extract the ZSR by
327   linear interpolation of the PPL points to the zenith position. In this situation, the cloud screening of PPL
328   points has been made checking the smoothness of the PPL curve as described in Holben et al. (1998). The
329   smoothness criterion analyses the second derivative of the PPL radiances with respect to the scattering
330   angle. This way the PPL measurement is classified as cloud contaminated if the second derivative is
331   negative (the threshold is not 0 but -1×10^{-7} as empirically determined) at any scattering angle between 2
332   and 90° (Almansa et al., 2020) The obtained ZSR from this method, based on the interpolation of cloud-
333   screened CE318 sky radiances measured in the PPL geometry, has been labelled as ZSR_{PPL}.

334   The PPL dataset is not directly available in the AERONET webpage; then, it has been extracted
335   from CAELIS database (Fuertes et al., 2018; González et al., 2020). ZSR_{ZEN} and ZSR_{PPL} measurements
336   within ± 1 min, are compared in Figure 6. Upper panels (a-d) of Figure 6 show the density scatter plots of
337   ZSR_{ZEN} against the reference ZSR_{PPL}, where a high correlation between both datasets can be observed for
338   all the channels, varying the determination coefficients from 0.94 at 870 nm to 0.99 at 440 and 500 nm. In
339   general, the number of outliers is higher for longer wavelengths.
340   In order to evaluate the uncertainty of the ZSR_{ZEN} measurements using ZSR_{PPL} as reference, the relative
341   differences between ZSR_{ZEN} and ZSR_{PPL} ($\Delta ZSR_{ZEN-PPL}$) have been evaluated and represented in frequency
342   histograms in the bottom panels (e-h) of Figure 6. These panels also include the mean (mean bias error;
343   MBE), median (Md) and standard deviation (SD) of $\Delta ZSR_{ZEN-PPL}$. The median values, less sensitive to
344   outliers, are close to zero (Md = 1.36%, -1.39% and -0.22% for 440, 500 and 675 nm, respectively)
345   indicating that the ZSR_{ZEN} are accurate regarding the reference ZSR_{PPL} values, except for 870 nm channel
346   which Md value of 4.99% points out an overestimation of the reference ZSR values. Nevertheless, the
347   precision decreases for longer wavelength channels, from SD values of 3.00% and 4.62% for 440 and 500
348   nm, respectively, to SD=12.54% and 21.37% for 675 and 870 nm.
349   All these statistical parameters have been calculated also considering the calibration coefficients,
350   without temperature correction, obtained at IARC with a calibrated integrating sphere. These parameters,
351   and the previously obtained by the proposed method of this work, are shown in Table 2 in order to observe
352   which calibration provide ZSR values closer to the reference ZSR_{PPL} values. The results of Table 2 show
353   that the ZSR obtained with the proposed calibration method, based on intercomparison with ZSR
354   simulations, is in general more accurate and precise except for 440 nm. Although the results of Table 2 for
355   440 nm are worse for the proposed calibration than for IARC calibration, the results are still good for the
356   proposed method with MBE close to 0 and a low value of SD. The ZSR_{ZEN} values from IARC calibration
357   are not temperature corrected, which could be behind of part of the observed differences.

358   All these results indicate that the ZSR_{ZEN} at 440 and 500 nm values are more accurate and precise than
359   at 675 and 870 nm. Then, ZSR_{ZEN} measurements at shorter wavelengths should have more weight in the
360   aerosol retrieval than the measured for longer ones, since measurements at 440 nm and 500 nm are more
361   trustable. The inversion module from GRASP code takes into account the weight of each measurement
362   through the so-called 'noises'; allowing to associate a different noise to each channel in this case. Therefore,

363 the obtained standard deviation of Table 2 (using the calibration proposed in this work), associated with the
364 ZSR_{ZEN} uncertainty, will be introduced for each channel in GRASP for the GRASP-ZEN method to account
365 for the different reliability of each channel.

4. Sensitivity analysis

367 In order to analyse the capabilities of the proposed inversion strategy to invert ZSR_{ZEN} measurements
368 with GRASP, a detailed sensitivity analysis is carried out in this section using synthetic data.
369 As mentioned in Section 2.2.2, the chosen method to obtain aerosols properties, considers five aerosol
370 types or 'models', which have fixed size distribution, refractive indices and sphere fraction. The method
371 must retrieve aerosol properties from measurements of ZSR_{ZEN} at 440, 500, 675 and 870nm. Sky radiances
372 depend on aerosol concentration and type, among other factors like the scattering angle and SZA; hence
373 they are commonly used to retrieve aerosol properties by measuring them at different scattering angles and
374 wavelengths (Nakajima et al., 1996; Román et al., 2022). Figure S4 shows in the supplementary material
375 the sky radiances in the zenith direction, modelled by GRASP for different aerosol concentrations, and how
376 they are sensitive to changes in the AOD and aerosol type for the five aerosol types used by the inversion
377 method. This figure shows that for higher SZA (Figure S4; panels i-l) the ZSR values are less sensitive to
378 aerosol type and concentration, since different scenarios show smaller differences in the corresponding
379 ZSR. Nevertheless, lower SZA conditions (Figure S4; panels a-d) show a clear sensitivity to type and
380 aerosol load for AOD at 440nm below 0.7, that would represent and extreme AOD event (Mateos et al.,
381 2020).
382 To explore the limitations of the retrieval of aerosol properties following the proposed inversion
383 strategy, two different tests have been carried out. For both tests, artificial aerosol scenarios have been
384 created and used as input to the GRASP forward module to simulate the ZSR that the ZEN-R52 would
385 register under these synthetic scenarios (ZSR_{SYN}). Since the ZSR_{SYN} values are artificially created, they will
386 be randomly perturbed following a Gaussian distribution defined by the uncertainty of each channel
387 previously calculated for the ZEN-R52 in order to create realistic observations (similar to Torres et al.,
388 2017 and Román et al., 2022, among others). The perturbed ZSR_{SYN} will be then used as input in the
389 inversion module, following the GRASP-ZEN method. It will provide the retrieved aerosol properties as
390 output, which will be labelled with the subindex 'INV' referring to 'inversion'. The test is focused on the
391 capability to retrieve AOD values and size distribution properties.

4.1. Scenarios from the combination of five aerosol types

393 This test creates random synthetic aerosol scenarios formed by a mixture of the five aerosol types
394 used by the 'models' GRASP inversion strategy (see Section 2.2.2). We aim here to assess the capabilities
395 of the retrieval of aerosol properties if the observed aerosol is actually a pure mixture of these five types of
396 aerosol. To this end, random fractions of each aerosol type are selected together with a random aerosol
397 concentration chosen in the interval from 0.01 to 0.15 $\mu m^3/\mu m^2$ creating a total of 1000 scenarios. The
398 simulations have been made for three different SZA values (30, 50 and 70°), but we will focus here in the
399 SZA=50° situation, which would represent a half-way and common scenario for the latitude of Valladolid.
400 Figure 7 shows the retrieved AOD (AOD_{INV}), using as input the perturbated ZSR_{ZEN} of each
401 created random scenario for SZA equal to 50°, against its original synthetic AOD value (AOD_{SYN}). The
402 same graphs for SZA values of 30° and 70° are shown in the Figure S5 of the supplementary material. In
403 general, the data deviation increases for high AOD values, which are less frequent. For SZA equal to 50°,
404 the method overestimates the aerosol load for all the wavelengths, with MBE ranging from 0.23 to 0.11.
405 The best results are obtained for SZA = 30°, with absolute mean bias errors lower than 0.002 for all
406 wavelengths and the lowest uncertainty (standard deviation lower than 0.66); while for SZA = 70° the
407 method slightly underestimates the AOD with MBEs ranging from -0.004 to 0. It is important to point out
408 that the convergence capability of the method decreases for high SZA, being the convergent inversions a
409 total of 43.2% and 43.6% at SZA=30° and 50° respectively but only 27.1% for SZA=70°; considering that
410 there are initially 1000 scenarios. These results could be related to the dependence of the ZSR sensitivity
411 on the SZA, which is higher for lower SZA, and therefore would make easier for the method to find a
412 solution.
413 For the size distribution the frequency histograms of the absolute differences between the inverted
414 and the synthetic parameters are shown in Figure 8 to have a clear overview of the results obtained (a direct
415 scatter plot comparison is shown in Figure S6). For the current synthetic test, the retrieval of size

416 distribution properties is very accurate and precise, showing Md values very close to zero for all the
417 properties. For the volume median radius the precision is high with SD < 10% for both fine and coarse
418 modes, but the precision is worse for the aerosol volume concentration with an SD value about 33.2% for
419 the total concentration. These results could be explained, at least in part, due to the fixed size distributions
420 for the 'models', which present similar RF, RC, σF and σC values and, therefore, it will not show an
421 important variation when combining them, but contrary, the aerosol volume concentration is an extensive
422 property and therefore can have a higher variation.

423 **4.2. AERONET scenarios**

424 The same procedure than in the previous test is developed in this one but using realistic aerosol
425 properties retrieved at Valladolid by AERONET. For this new test, all the available inversions (almucantar
426 and hybrid scans) from AERONET for the coincident ZEN-R52 measurement period (2019-2021) with and
427 sky error < 5% have been obtained, achieving a total of 5321 synthetic scenarios. With this test we aim to
428 assess the capabilities of the method to retrieve the aerosol properties when the ZSR come from an aerosol
429 scenario closer to real aerosol conditions and not necessarily to a mixture of the five mentioned aerosol
430 types. In this situation the ZSR_{SYN} simulations are made for the corresponding date and time at which the
431 AERONET inversion product was retrieved, achieving a wide variety of SZA values (18°<SZA<78°).

432 Figure 9 presents the comparison between the AOD_{INV}, obtained from the inversion of the
433 perturbed ZSR_{SYN} as input in GRASP-ZEN method, and AOD_{SYN} for these AERONET synthetic scenarios.
434 This comparison reveals a clear overestimation of the inverted AOD values compared to the original ones
435 for the four wavelengths, ranging the MBE values from 0.01 to 0.04 and the Md from 0.01 to 0.03 for the
436 differences between both datasets. These results could be related with the previous results for overestimated
437 AOD at SZA = 50°, but in this situation the overestimation is not related to the SZA since it has been
438 checked that points with different SZA are homogeneously distributed, therefore AOD_{SYN} is always
439 overestimated by the obtained from GRASP-ZEN for all SZA. The standard deviation of the AOD
440 differences, which can be associated with the uncertainty in AOD_{INV}, is above 0.02, being 0.05 for 440 and
441 500 nm, which are higher than the standard deviation obtained in the previous section for all wavelengths
442 and SZAs, SD = 0.090 (for AOD 440 nm at SZA=50°).

443 The reason for the observed overestimation could be in the limitations of the GRASP-ZEN method
444 based on the 'models' approach, which only allows to retrieve aerosol properties within the properties of
445 the five aerosol types. It means that, for example, if the real aerosol has a median radius of fine mode bigger
446 than the ones of the five 'models', then the GRASP-ZEN retrieval will underestimate the real median radius
447 of fine mode and this difference will be compensated unbalancing other aerosol properties to fit the
448 measured ZSR and the synthetic ZSR values of the retrieved aerosol scenario (to reduce the residual
449 differences in ZSR values).

450 To explore this hypothesis, the retrieved size distribution properties have been compared with the
451 synthetic ones. The frequency histograms for the absolute differences between the inverted and the
452 synthetic properties are shown in Figure 10 (the direct scatter plot comparison can be seen in Figure S7).
453 The retrieved volume concentrations present median differences regarding the synthetic ones about
454 0.01μm³/μm² for VCF and VCT, while this median value is close to zero for the VCC. The retrieved fine
455 intensive properties underestimate the reference values, being the median values of their differences about
456 -14% and -10% for RF and σF, respectively, and -10% and -4% for RC and σC, respectively.

457 This lack of accuracy is the main difference between the results of Figure 10 and Figure 8. As
458 mentioned before, we would expect a big accuracy and precision in the retrieved values of the volume
459 median radius and standard deviation for the 'models' combination scenarios test (Section 4.1), since the
460 scenario can be perfectly reproduced by GRASP-ZEN because it is a combination of the same models used
461 in the inversion module; however, for a real aerosol scenario (the test for AERONET scenarios of this
462 subsection), these properties could be impossible to obtain with enough accuracy since they present wider
463 range of size distributions than the offered by the 'models' approach. Similar results are expected for the
464 real and imaginary refractive index and other optical properties, due to the limitations of the 'models'
465 approach.

466 The results of this section conclude that the GRASP-ZEN method is useful for the retrieval of
467 AOD but nor for some size distribution properties, like the volume median radius and standard deviation

468 of fine and coarse modes. Therefore, we will focus on the retrieval of AOD at 440, 500, 675 and 870 nm
469 and VCF, VCC and VCT.

470 ## 5. Results

471 Once the ZSR_{ZEN} measurements have been obtained from ZEN-R52 by the calibration method
472 proposed in Section 3, and the GRASP-ZEN method has been proved in Section 4 as capable to retrieve
473 some aerosol properties like AOD, the GRASP-ZEN methodology has been applied to all the available
474 dataset from ZEN-R52 measurements at Valladolid, obtaining a total of 222663 GRASP-ZEN retrievals.
475 This dataset has been obtained using ZSR_{ZEN} measurements which satisfy the filtering criteria, regarding
476 SZA and ZEN error, determined in Section 3.2. The retrievals which do not present enough convergence
477 have been removed, which led to a total of 170637 retrievals. This convergence check is based on the
478 residuals of the inversion process (see Section 2.2.2). A cloud-screening filter is applied, based mainly on
479 the retrieved AOD at 500 nm, following a similar procedure as Giles et al. (2019) for cloud-screening in
480 AERONET version 3. Three checks are applied for this cloud-screening: smoothness, stand-alone and $\pm3\sigma$.
481 The smoothness check is done by the analysis of the AOD variation at 500 nm: for each two subsequent
482 values if the variation is higher than 0.01/min the retrieval with larger AOD at 500 nm in the pair is removed.
483 After the smoothness, the stand-alone check is applied: all single retrievals remaining which are more than
484 1 hour apart from the closest available retrieval are removed. Finally, for each day the daily mean and
485 standard deviation are calculated for the retrieved AOD at 500 nm and for the Ångström Exponent (AE;
486 Ångström, 1964) obtained with the four retrieved AOD values (440, 500, 676 and 870 nm). To satisfy the
487 $\pm3\sigma$ check, the retrieved AOD at 500 nm and AE must be within the daily mean $\pm3\sigma$ (triple standard
488 deviation). Values not satisfying this requirement are removed. A final dataset with 126112 points
489 satisfying the convergence and cloud-screening criteria is obtained.

490 ### 5.1 Aerosol Optical Depth

491 The AOD retrieved by GRASP-ZEN using the ZSR_{ZEN} measurements (AOD_{GRASP_ZEN}) has been
492 compared against independent AOD measurements from AERONET ($AOD_{AERONET}$) derived from CE318
493 sun-sky photometers collocated with the ZEN-R52 at Valladolid. Figure 11 shows the complete time series
494 evolution of AOD_{GRASP_ZEN} together with $AOD_{AERONET}$, both at 440 nm. Despite some AOD_{GRASP_ZEN}
495 outbreaks which are not reproduced by the $AOD_{AERONET}$, both datasets show in general a similar temporal
496 evolution. Figure 12 shows a more detailed view of these these data in a shorter period, from 16 to 22 June 2020,
497 with high availability of data from both GRASP-ZEN and AERONET datasets for the four available
498 wavelengths. A lack of AOD values in the GRASP-ZEN dataset around mid-day is observed; it is explained
499 by the rejection of ZEN-R52 measurements for SZA below 30°, which, in the analysed period and latitude,
500 occurs around mid-day. In Figure 12 (panels a–d) it can be also observed that both GRASP-ZEN and
501 AERONET datasets vary with time in a similar way for all the wavelengths, with AOD values from
502 GRASP-ZEN slightly overestimating the AOD values from AERONET at all wavelengths. Figure 12 (panel
503 e) includes the AOD_{GRASP_ZEN} at 440, 500, 675 and 870 nm in the same plot, showing the behaviour
504 expected for the AOD at these wavelengths: AOD decreasing with wavelength and parallel time evolution.
505 To perform a more quantitative analysis of the correlation between these datasets, a match-up of
506 AERONET AOD ($AOD_{AERONET}$) data with GRASP-ZEN AOD (AOD_{GRASP_ZEN}) values within 1.5 minutes
507 has been made, obtaining a total of 37787 coincident points per wavelength. The AOD data from GRASP-
508 ZEN is represented against the coincident AOD from AERONET in a density plot in Figure 13 for each
509 wavelength (panels a- d). This figure (panels e-h) also shows in the bottom panels the frequency histograms
510 of the differences between both AOD datasets. AOD_{GRASP_ZEN} presents a higher correlation with
511 $AOD_{AERONET}$ for shorter wavelengths, ranging r^2 from 0.86 at 440 nm to 0.72 at 870 nm. In general, the
512 AOD at 675 nm, and especially at 870 nm, presents more deviation between the data pairs than for the
513 shorter wavelengths. Some outliers presenting high AOD_{GRASP_ZEN} values can be appreciated, especially at
514 shorter wavelengths; it could be caused by some spurious measurements likely contaminated by clouds that
515 pass the cloud-screening criteria, or recorded with dirtiness, rain droplets or dust over the instrument (it
516 must be frequently cleaned). AOD from GRASP-ZEN generally overestimates the AERONET values, as
517 synthetic study of Section 4.2 points out, with median values of the differences of AOD_{GRASP_ZEN} with
518 respect to $AOD_{AERONET}$ between 0.01 and 0.02 for all wavelengths; similar values appear for MBE, ranging
519 from 0.01 to 0.03. The uncertainty in the retrieved AOD_{GRASP_ZEN} is estimated by SD to be 0.03 for 440 and
520 500 nm and 0.02 for 675 and 870 nm using as reference the values provided by AERONET.

521   5.2 Aerosol volume concentration

522   Regarding the total aerosol volume concentration, the retrieved values with GRASP-ZEN and the
523 obtained from AERONET along the analysed period are shown in Figure 14. The time evolution shows
524 generally a similar behaviour for both datasets with exception of some VCT extreme values more frequent
525 in the GRASP-ZEN database. Here it can be also seen that for this parameter there is a higher temporal
526 coverage from GRASP-ZEN than from AERONET. This is because unlike the AOD, which is obtained
527 from direct irradiance measurements, usually carried out every 3 minutes, the aerosol volume concentration
528 is obtained from AERONET inversion products, which are retrieved from the combination of AOD and
529 sky radiance measurements. Sky radiances are performed less frequently than the direct sun ones, and
530 inversions are only processed if the sky measurements are available and satisfy certain requirements
531 (Sinyuk et al., 2020).
532   The VCT, VCC and VCC values from both datasets are shown in Figure 15 for the week from 16 to
533 22 June 2020 (same days than Figure 12), showing again a similar behaviour for the two datasets. Figure
534 15 also reveals that the GRASP-ZEN values are noisier and overestimates the AERONET values, especially
535 for the fine mode.
536   In order to perform a quantitative analysis for the correlation between VCT, VCC and VCC from
537 GRASP-ZEN and AERONET datasets a match-up has been done. In this case, the GRASP-ZEN values
538 closest to the AERONET values within 5 minutes are chosen, obtaining a total of 4356 coincident points
539 for each volume concentration. A higher temporal range is selected here because the inversion products are
540 less frequent than AOD. In addition, we assume that these aerosol properties should not change significantly
541 in 5 minutes.
542   The GRASP-ZEN volume concentrations are represented against the coincident AERONET ones in
543 the density scatter plots of the upper panels of Figure 16 for fine, coarse and total values. Bottom panels of
544 Figure 16 also show the frequency histograms of the differences between GRASP-ZEN and AERONET
545 values of VCF, VCC and VCT. The best correlation is obtained for the total volume concentration with a
546 r^2 about 0.66, while for fine and coarse volume concentration the determination coefficient is 0.57 and 0.56,
547 respectively. Despite the lower correlation coefficients, the retrieved volume concentrations are rather
548 precise with values of the median of the differences between GRASP-ZEN and AERONET datasets about
549 0.006 and 0.005 $\mu m^3/\mu m^2$ for fine and coarse modes, respectively, and 0.010 $\mu m^3/\mu m^2$ for the VCT. The
550 highest uncertainty on the retrieved volume concentrations is in the VCT, which presents a SD value about
551 0.20 $\mu m^3/\mu m^2$; while for fine and coarse modes these values are 0.009 $\mu m^3/\mu m^2$ and 0.016 $\mu m^3/\mu m^2$, which
552 are close to the uncertainty offered by AERONET, 0.01 $\mu m^3/\mu m^2$.

553   All of the results of this paper have been obtained using the GRASP-ZEN methodology based on the
554 'models' approach, which is a suitable option for the current issue due to the reduced number of radiometric
555 observations provided by the ZEN-R52. However, the versatility of GRASP code allows different strategies
556 for the retrieval of aerosol properties. In this sense, we have considered other strategies in this study to
557 choose the one which provides the best results. These strategies are based on the temporal multi-pixel
558 approach offered by GRASP (Lopatin et al., 2021), that constraints the variation of aerosol properties in
559 time, forcing them to vary smoothly. The multi-pixel approach was firstly used in combination with the
560 'models' approach. In order to avoid the problems derived of having fixed aerosol models with fixed aerosol
561 properties, the temporal multi-pixel was also used assuming the size distribution as a bimodal (fine and
562 coarse modes) log-normal distribution and the refractive indices have no dependence on wavelength. None
563 of the methods improved the retrieval of aerosol properties but slightly reduce it; likely due to the intrusion
564 of contaminated measurements that influenced the retrieval, but they did reduce the computation time (the
565 data of a full day are inverted all at the same time). Nevertheless, these strategies could be considered for
566 future aerosol retrievals.

567   6.   Conclusions

568   This paper has explored the capabilities to calibrate a ZEN-R52 radiometer using the GRASP
569 (Generalized Retrieval of Atmosphere and Surface Properties) code and to retrieve aerosol properties from
570 measured zenith sky radiances (ZSR) at four wavelengths. The ZSR values measured by the ZEN-R52
571 radiometer for solar zenith angle (SZA) values below 30° are contaminated by stray sun light intromission
572 and, hence, should not be used. For some latitudes this would result in the absence of measurements for

most of the time, and therefore a technical improvement in the instrument to correct this issue is recommended to the manufacturers.

The proposed methodology for the calibration of ZEN-R52, using simulated ZSR values has been contrasted, showing discrepancies lower than 6% respect to the calibration coefficients obtained against an integrating sphere. This proposed methodology incorporates the advantage that it includes the normalization used by GRASP and therefore there is not any need to use extraterrestrial spectra to normalize the data when they are used as input in GRASP.

A new inversion strategy, called GRASP-ZEN, has been proposed to retrieve aerosol properties with GRASP code using the ZSR values measured by ZEN-R52. An analysis with synthetic data has concluded that ZSR measurements are useful to derive aerosol optical depth (AOD), since these measurements are sensitive to aerosol load and type for the ZEN-R52 channels, at least for AOD at 440 nm below 1. This sensitivity decreases when SZA increases due to the decrease on the intensity of the ZSR values. A couple of tests with synthetic data have revealed that the GRASP-ZEN inversion strategy generally overestimates the AOD for all channels under real aerosol scenarios.

The GRASP-ZEN method has been applied to ZSR measurements recorded with a ZEN-R52 radiometer at Valladolid (Spain) for two years and half. A direct comparison of some retrieved aerosol properties against independent AERONET (Aerosol Robotic Network) products has pointed out the accuracy and precision of the aerosol properties retrieved by GRASP-ZEN. The correlation between the AOD retrieved by GRASP-ZEN and AERONET is high, with determination coefficients (r^2) about 0.86, 0.85, 0.79 and 0.72 for 440, 500, 675 and 870 nm, respectively. The uncertainties on the retrieved AOD values are between ±0.02 and ±0.03 considering the AERONET values as reference. AERONET offers uncertainties about ±0.01 for wavelengths above 440 nm, and therefore the uncertainty achieved by the proposed method is higher that the offered by the reference value.

With respect other aerosol properties, the GRASP-ZEN retrieval is limited for the intensive properties, like complex refractive index and some size distribution parameters due to the use of the 'models' approach of GRASP. Nevertheless, the retrieved volume concentrations, which are extensive properties, have been compared against the same independent AERONET products to quantify the relative accuracy and precision in these concentrations retrieved by GRASP-ZEN. The r^2 obtained comparing the volume concentrations obtained with GRASP-ZEN with respect to the AERONET reference values show low values for the fine (0.57) and coarse (0.56) modes, while for the total volume concentration a higher value (0.66) has been obtained. Nevertheless, the median and standard deviation of the differences on volume concentration between GRASP-ZEN and AERONET are lower than 0.01 $\mu m^3/\mu m^2$ and 0.02 $\mu m^3/\mu m^2$, respectively, for both fine and coarse mode and also total concentration. These results have indicated that GRASP-ZEN is capable to retrieve the aerosol volume concentrations with good accuracy and precision.

This paper shows the potential of a simple and robust radiometer like the ZEN-R52 as a possible alternative for aerosol properties retrieval in remote areas. The proposed methodology would require of a previous coincident period of measurements collocated with an AERONET CE318 photometer to achieve the calibration, and later could be deployed in a remote site in order to broaden the aerosol monitoring network. This paper also assesses the capability from GRASP to retrieve aerosol properties using only ZSR at 440, 500, 675 and 870 nm. The uncertainty and bias found in the retrieval show the limitations of the instrument and inversion strategy, but also demonstrate that the ZEN-R52, together with the developed GRASP-ZEN strategy, can provide useful information about the AOD and aerosol volume concentration for total, fine and coarse modes. This can be especially useful for remote areas or even in places with collocated a CE318 photometer in order to increase the time resolution.

Acknowledgments

This research has been supported by the Ministerio de Ciencia e Innovación (grant no. PID2021-127588OB-I00), the Junta de Castilla y León (grant no. VA227P20). This publication is part of the TED2021-131211B-I00 project funded by MCIN/AEI/10.13039/501100011033 and European Union "NextGenerationEU"/PRTR. This article is based upon work from COST Action CA21119 HARMONIA, supported by COST (European Cooperation in Science and Technology) and has been supported by the European Metrology Program for Innovation and Research (EMPIR) within the joint research project EMPIR 19ENV04 MAPP. We especially thank the GOA-UVa staff members (Rogelio Carracedo, Patricia Martín-Sánchez and Javier Gatón), for helping with the research through the maintenance of the instruments and the station infrastructure.

References

Almansa, A. F., Cuevas, E., Barreto, Á., Torres, B., García, O. E., García, R. D., Velasco-Merino, C., Cachorro, V. E., Berjón, A., Mallorquín, M., López, C., Ramos, R., Guirado-Fuentes, C., Negrillo, R., & de Frutos, Á. M. (2020). Column integrated water vapor and aerosol load characterization with the new ZEN-R52 radiometer. Remote Sensing, 12(9). https://doi.org/10.3390/RS12091424

Almansa, A. F., Cuevas, E., Torres, B., Barreto, Á., García, R. D., Cachorro, V. E., De Frutos, Á. M., López, C., & Ramos, R. (2017). A new zenith-looking narrow-band radiometer-based system (ZEN) for dust aerosol optical depth monitoring. Atmospheric Measurement Techniques, 10(2), 565–579. https://doi.org/10.5194/AMT-10-565-2017

Ångström, A. (1964). The parameters of atmospheric turbidity. Tellus, 16(1), 64–75. https://doi.org/10.1111/J.2153-3490.1964.TB00144.X

Barker, H. W., & Marshak, A. (2001). Inferring Optical Depth of Broken Clouds above Green Vegetation Using Surface Solar Radiometric Measurements. Journal of the Atmospheric Sciences, 58(20), 2989–3006. https://doi.org/10.1175/1520-0469(2001)058<2989:IODOBC>2.0.CO;2

Barreto, Á., Cuevas, E., Granados-Muñoz, M. J., Alados-Arboledas, L., Romero, P. M., Gröbner, J., Kouremeti, N., Almansa, A. F., Stone, T., Toledano, C., Román, R., Sorokin, M., Holben, B., Canini, M., & Yela, M. (2016). The new sun-sky-lunar Cimel CE318-T multiband photometer – A comprehensive performance evaluation. Atmospheric Measurement Techniques, 9(2), 631–654. https://doi.org/10.5194/AMT-9-631-2016

Barreto, A., Román, R., Cuevas, E., Pérez-Ramírez, D., Berjón, A. J., Kouremeti, N., Kazadzis, S., Gröbner, J., Mazzola, M., Toledano, C., Benavent-Oltra, J. A., Doppler, L., Juryšek, J., Almansa, A. F., Victori, S., Maupin, F., Guirado-Fuentes, C., González, R., Vitale, V., … Yela, M. (2019). Evaluation of night-time aerosols measurements and lunar irradiance models in the frame of the first multi-instrument nocturnal intercomparison campaign. Atmospheric Environment, 202, 190–211. https://doi.org/10.1016/J.ATMOSENV.2019.01.006

Benavent-Oltra, J. A., Román, R., Andrés Casquero-Vera, J., Pérez-Ramírez, D., Lyamani, H., Ortiz-Amezcua, P., Bedoya-Velásquez, A. E., De Arruda Moreira, G., Barreto, Á., Lopatin, A., Fuertes, D., Herrera, M., Torres, B., Dubovik, O., Luis Guerrero-Rascado, J., Goloub, P., Olmo-Reyes, F. J., & Alados-Arboledas, L. (2019). Different strategies to retrieve aerosol properties at night-time with the GRASP algorithm. Atmospheric Chemistry and Physics, 19(22), 14149–14171. https://doi.org/10.5194/ACP-19-14149-2019

Benavent-Oltra, J. A., Román, R., Granados-Munõz, M. J., Pérez-Ramírez, D., Ortiz-Amezcua, P., Denjean, C., Lopatin, A., Lyamani, H., Torres, B., Guerrero-Rascado, J. L., Fuertes, D., Dubovik, O., Chaikovsky, A., Olmo, F. J., Mallet, M., & Alados-Arboledas, L. (2017). Comparative assessment of GRASP algorithm for a dust event over Granada (Spain) during ChArMEx-ADRIMED 2013 campaign. Atmospheric Measurement Techniques, 10(11), 4439–4457. https://doi.org/10.5194/AMT-10-4439-2017

Bennouna, Y. S., Cachorro, V. E., Torres, B., Toledano, C., Berjón, A., de Frutos, A. M., & Alonso Fernández Coppel, I. (2013). Atmospheric turbidity determined by the annual cycle of the aerosol

668   optical depth over north-center Spain from ground (AERONET) and satellite (MODIS).
669   Atmospheric Environment, 67, 352–364. https://doi.org/10.1016/J.ATMOSENV.2012.10.065

670   Boucher, O., Randall, D., Artaxo, P., Bretherton, C., Feingold, G., Forster, P., Kerminen, V., Kondo, Y.,
671   Liao, H., Lohmann, U., Rasch, P., Satheesh, S., Sherwood, S., Stevens, B., & Zhang, X. (2013).
672   Clouds and Aerosols. In: Climate Change 2013: The Physical Science Basis. Contribution of
673   Working Group I to the Fifth Assessment Report of the Intergovernmental Panel on Climate
674   Change Coordinating Lead Authors: Lead Authors.
675   https://doi.org/10.1017/CBO9781107415324.016

676   Cachorro, V. E., Burgos, M. A., Mateos, D., Toledano, C., Bennouna, Y., Torres, B., De Frutos, Á. M., &
677   Herguedas, Á. (2016). Inventory of African desert dust events in the north-central Iberian Peninsula
678   in 2003-2014 based on sun-photometer-AERONET and particulate-mass-EMEP data. Atmospheric
679   Chemistry and Physics, 16(13), 8227–8248. https://doi.org/10.5194/ACP-16-8227-2016

680   Chen, C., Dubovik, O., Fuertes, D., Litvinov, P., Lapyonok, T., Lopatin, A., Ducos, F., Derimian, Y.,
681   Herman, M., Tanré, D., Remer, L. A., Lyapustin, A., Sayer, A. M., Levy, R. C., Christina Hsu, N.,
682   Descloitres, J., Li, L., Torres, B., Karol, Y., … Federspiel, C. (2020). Validation of GRASP
683   algorithm product from POLDER/PARASOL data and assessment of multi-angular polarimetry
684   potential for aerosol monitoring. Earth System Science Data, 12(4), 3573–3620.
685   https://doi.org/10.5194/ESSD-12-3573-2020

686   Chiu, C. J., Huang, C.-H., Marshak, A., Slutsker, I., Giles, D. M., Holben, B. N., Knyazikhin, Y.,
687   Wiscombe, W. J., Huang, C., Marshak, A., Slutsker, I., Giles, D. M., Holben, B. N., Knyazikhin,
688   Y., & Wiscombe, W. J. (2010). Cloud optical depth retrievals from the Aerosol Robotic Network
689   (AERONET) cloud mode observations. Journal of Geophysical Research: Atmospheres, 115(D14),
690   14202. https://doi.org/10.1029/2009JD013121

691   Cissé, G., McLeman, R., Adams, H., Aldunce, P., Bowen, K., Campbell-Lendrum, D., Clayton, S., Ebi,
692   K. L., Hess, J., Huang, C., Liu, Q., McGregor, G., Semenza, J., & Tirado, M. C. (2022). Health,
693   Wellbeing, and the Changing Structure of Communities. In: Climate Change 2022: Impacts,
694   Adaptation, and Vulnerability. Contribution of Working Group II to the Sixth Assessment Report of
695   the Intergovernmental Panel on Climate Change [H.-O. Pörtner, D.C. Roberts, M. Tignor, E.S.
696   Poloczanska, K. Mintenbeck, A. Alegría, M. Craig, S. Langsdorf, S. Löschke, V. Möller, A. Okem,
697   B. Rama (eds.)]. https://doi.org/10.1017/9781009325844.008.

698   Dubovik, O., Fuertes, D., Litvinov, P., Lopatin, A., Lapyonok, T., Doubovik, I., Xu, F., Ducos, F., Chen,
699   C., Torres, B., Derimian, Y., Li, L., Herreras-Giralda, M., Herrera, M., Karol, Y., Matar, C.,
700   Schuster, G. L., Espinosa, R., Puthukkudy, A., … Federspiel, C. (2021). A Comprehensive
701   Description of Multi-Term LSM for Applying Multiple a Priori Constraints in Problems of
702   Atmospheric Remote Sensing: GRASP Algorithm, Concept, and Applications. Frontiers in Remote
703   Sensing, 2, 23. https://doi.org/10.3389/FRSEN.2021.706851

704   Dubovik, O., & King, M. D. (2000). A flexible inversion algorithm for retrieval of aerosol optical
705   properties from Sun and sky radiance measurements. Journal of Geophysical Research:
706   Atmospheres, 105(D16), 20673–20696. https://doi.org/10.1029/2000JD900282

707   Dubovik, O., Lapyonok, T., Litvinov, P., Herman, M., Fuertes, D., Ducos, F., Torres, B., Derimian, Y.,
708   Huang, X., Lopatin, A., Chaikovsky, A., Aspetsberger, M., & Federspiel, C. (2014). GRASP: a
709   versatile algorithm for characterizing the atmosphere. SPIE Newsroom.
710   https://doi.org/10.1117/2.1201408.005558

711   Eilers, P. H. C., & Goeman, J. J. (2004). Enhancing scatterplots with smoothed densities. Bioinformatics,
712   20(5), 623–628. https://doi.org/10.1093/BIOINFORMATICS/BTG454

713   Espinosa, W. R., Remer, L. A., Dubovik, O., Ziemba, L., Beyersdorf, A., Orozco, D., Schuster, G.,
714   Lapyonok, T., Fuertes, D., & Vanderlei Martins, J. (2017). Retrievals of aerosol optical and
715   microphysical properties from Imaging Polar Nephelometer scattering measurements. Atmospheric
716   Measurement Techniques, 10(3), 811–824. https://doi.org/10.5194/AMT-10-811-2017

717   Fuertes, D., Toledano, C., González, R., Berjón, A., Torres, B., Cachorro, V. E., & De Frutos, Á. M.
718   (2018). CÆLIS: Software for assimilation, management and processing data of an atmospheric
719   measurement network. Geoscientific Instrumentation, Methods and Data Systems, 7(1), 67–81.
720   https://doi.org/10.5194/GI-7-67-2018

721   Giles, D. M., Sinyuk, A., Sorokin, M. G., Schafer, J. S., Smirnov, A., Slutsker, I., Eck, T. F., Holben, B.
722   N., Lewis, J. R., Campbell, J. R., Welton, E. J., Korkin, S. V., & Lyapustin, A. I. (2019).
723   Advancements in the Aerosol Robotic Network (AERONET) Version 3 database - Automated near-
724   real-time quality control algorithm with improved cloud screening for Sun photometer aerosol
725   optical depth (AOD) measurements. Atmospheric Measurement Techniques, 12(1), 169–209.
726   https://doi.org/10.5194/AMT-12-169-2019

727   González, R., Toledano, C., Román, R., Fuertes, D., Berjón, A., Mateos, D., Guirado-Fuentes, C.,
728   Velasco-Merino, C., Antuña-Sánchez, J. C., Calle, A., Cachorro, V. E., & De Frutos, Á. M. (2020).
729   Daytime and nighttime aerosol optical depth implementation in CÆLIS. Geoscientific
730   Instrumentation, Methods and Data Systems, 9(2), 417–433. https://doi.org/10.5194/GI-9-417-2020

731   Herreras, M., Román, R., Cazorla, A., Toledano, C., Lyamani, H., Torres, B., Cachorro, V. E., Olmo, F.
732   J., Alados-Arboledas, L., & de Frutos, A. M. (2019). Evaluation of retrieved aerosol extinction
733   profiles using as reference the aerosol optical depth differences between various heights.
734   Atmospheric Research, 230, 104625. https://doi.org/10.1016/J.ATMOSRES.2019.104625

735   Herreras-Giralda, M., Litvinov, P., Dubovik, O., Derimian, Y., Lapyonok, T., Fuertes, D., Sourdeval, O.,
736   Preusker, R., & Fischer, J. (2022). Thermal emission in the successive orders of scattering (SOS)
737   radiative transfer approach. Journal of Quantitative Spectroscopy and Radiative Transfer, 291,
738   108327. https://doi.org/10.1016/J.JQSRT.2022.108327

739   Holben, B. N., Eck, T. F., Slutsker, I., Tanré, D., Buis, J. P., Setzer, A., Vermote, E., Reagan, J. A.,
740   Kaufman, Y. J., Nakajima, T., Lavenu, F., Jankowiak, I., & Smirnov, A. (1998). AERONET—A
741   Federated Instrument Network and Data Archive for Aerosol Characterization. Remote Sensing of
742   Environment, 66(1), 1–16. https://doi.org/10.1016/S0034-4257(98)00031-5

743   Lenoble, J., Herman, M., Deuzé, J. L., Lafrance, B., Santer, R., & Tanré, D. (2007). A successive order of
744   scattering code for solving the vector equation of transfer in the earth's atmosphere with aerosols.
745   Journal of Quantitative Spectroscopy and Radiative Transfer, 107(3), 479–507.
746   https://doi.org/10.1016/J.JQSRT.2007.03.010

747   Lopatin, A., Dubovik, O., Chaikovsky, A., Goloub, P., Lapyonok, T., Tanré, D., & Litvinov, P. (2013).
748   Enhancement of aerosol characterization using synergy of lidar and sun-photometer coincident
749   observations: The GARRLiC algorithm. Atmospheric Measurement Techniques, 6(8), 2065–2088.
750   https://doi.org/10.5194/AMT-6-2065-2013

751   Lopatin, A., Dubovik, O., Fuertes, D., Stenchikov, G., Lapyonok, T., Veselovskii, I., Wienhold, F. G.,
752   Shevchenko, I., Hu, Q., & Parajuli, S. (2021). Synergy processing of diverse ground-based remote
753   sensing and in situ data using the GRASP algorithm: applications to radiometer, lidar and
754   radiosonde observations. Atmospheric Measurement Techniques, 14(3), 2575–2614.
755   https://doi.org/10.5194/AMT-14-2575-2021

756   Marshak, A., Knyazikhin, Y., Davis, A. B., Wiscombe, W. J., & Pilewskie, P. (2000). Cloud-vegetation
757   interaction: Use of normalized difference cloud index for estimation of cloud optical thickness.
758   Geophysical Research Letters, 27(12), 1695–1698. https://doi.org/10.1029/1999GL010993

759   Mateos, D., Cachorro, V. E., Velasco-Merino, C., O'Neill, N. T., Burgos, M. A., Gonzalez, R., Toledano,
760   C., Herreras, M., Calle, A., & de Frutos, A. M. (2020). Comparison of three different
761   methodologies for the identification of high atmospheric turbidity episodes. Atmospheric Research,
762   237, 104835. https://doi.org/10.1016/j.atmosres.2019.104835

763   Molero, F., Pujadas, M., & Artíñano, B. (2020). Study of the Effect of Aerosol Vertical Profile on
764   Microphysical Properties Using GRASP Code with Sun/Sky Photometer and Multiwavelength

765 Lidar Measurements. Remote Sensing 2020, Vol. 12, Page 4072, 12(24), 4072.
766 https://doi.org/10.3390/RS12244072

767 Myhre, G., Shindell, D., Bréon, F., Collins, W., Fuglestvedt, J., Huang, J., Koch, D., Lamarque, J., Lee,
768 D., Mendoza, B., Nakajima, T., Robock, A., Stephens, G., Takemura, T., & Zhang, H. (2013).
769 Anthropogenic and Natural Radiative Forc-ing. In: Climate Change 2013: The Physical Science
770 Basis. Contribution of Working Group I. https://doi.org/10.1017/CBO9781107415324.018

771 Nakajima, T., Tonna Glauco, Rao, R., Boi, P., Kaufman, Y., & Holben, B. (1996). Use of sky brightness
772 measurements from ground for remote sensing of particulate polydispersions. Applied Optics, Vol.
773 35, Issue 15, Pp. 2672-2686, 35(15), 2672–2686. https://doi.org/10.1364/AO.35.002672

774 Román, R., Antuña-Sánchez, J. C., Cachorro, V. E., Toledano, C., Torres, B., Mateos, D., Fuertes, D.,
775 López, C., González, R., Lapionok, T., Herreras-Giralda, M., Dubovik, O., & De Frutos, Á. M.
776 (2022). Retrieval of aerosol properties using relative radiance measurements from an all-sky
777 camera. Atmospheric Measurement Techniques, 15(2), 407–433. https://doi.org/10.5194/AMT-15-
778 407-2022

779 Román, R., Benavent-Oltra, J. A., Casquero-Vera, J. A., Lopatin, A., Cazorla, A., Lyamani, H., Denjean,
780 C., Fuertes, D., Pérez-Ramírez, D., Torres, B., Toledano, C., Dubovik, O., Cachorro, V. E., de
781 Frutos, A. M., Olmo, F. J., & Alados-Arboledas, L. (2018). Retrieval of aerosol profiles combining
782 sunphotometer and ceilometer measurements in GRASP code. Atmospheric Research, 204, 161–
783 177. https://doi.org/10.1016/J.ATMOSRES.2018.01.021

784 Román, R., Bilbao, J., & de Miguel, A. (2014). Reconstruction of six decades of daily total solar
785 shortwave irradiation in the Iberian Peninsula using sunshine duration records. Atmospheric
786 Environment, 99, 41–50. https://doi.org/10.1016/J.ATMOSENV.2014.09.052

787 Román, R., González, R., Toledano, C., Barreto, Á., Pérez-Ramírez, D., Benavent-Oltra, J. A., Olmo, F.
788 J., Cachorro, V. E., Alados-Arboledas, L., & de Frutos, Á. M. (2020). Correction of a lunar-
789 irradiance model for aerosol optical depth retrieval and comparison with a star photometer.
790 Atmospheric Measurement Techniques, 13(11), 6293–6310. https://doi.org/10.5194/AMT-13-6293-
791 2020

792 Román, R., Torres, B., Fuertes, D., Cachorro, V. E., Dubovik, O., Toledano, C., Cazorla, A., Barreto, A.,
793 Bosch, J. L., Lapyonok, T., González, R., Goloub, P., Perrone, M. R., Olmo, F. J., de Frutos, A., &
794 Alados-Arboledas, L. (2017). Remote sensing of lunar aureole with a sky camera: Adding
795 information in the nocturnal retrieval of aerosol properties with GRASP code. Remote Sensing of
796 Environment, 196, 238–252. https://doi.org/10.1016/J.RSE.2017.05.013

797 Schaaf, C., Liu, J., Gao, F., & Strahler, A. H. (2011). MODIS albedo and reflectance anisotropy products
798 from Aqua and Terra, Land Remote Sensing and Global Environmental Change: NASA's Earth
799 Observing System and the Science of ASTER and MODIS. 11, 549–561.

800 Sinyuk, A., Sinyuk, A., Holben, B. N., Eck, T. F., Eck, T. F., M. Giles, D., M. Giles, D., Slutsker, I.,
801 Slutsker, I., Korkin, S., Korkin, S., S. Schafer, J., S. Schafer, J., Smirnov, A., Smirnov, A., Sorokin,
802 M., Sorokin, M., & Lyapustin, A. (2020). The AERONET Version 3 aerosol retrieval algorithm,
803 associated uncertainties and comparisons to Version 2. Atmospheric Measurement Techniques,
804 13(6), 3375–3411. https://doi.org/10.5194/AMT-13-3375-2020

805 Titos, G., Ealo, M., Román, R., Cazorla, A., Sola, Y., Dubovik, O., Alastuey, A., & Pandolfi, M. (2019).
806 Retrieval of aerosol properties from ceilometer and photometer measurements: Long-term
807 evaluation with in situ data and statistical analysis at Montsec (southern Pyrenees). Atmospheric
808 Measurement Techniques, 12(6), 3255–3267. https://doi.org/10.5194/AMT-12-3255-2019

809 Torres, B., Dubovik, O., Fuertes, D., Schuster, G., Eugenia Cachorro, V., Lapyonok, T., Goloub, P.,
810 Blarel, L., Barreto, A., Mallet, M., Toledano, C., & Tanré, D. (2017). Advanced characterisation of
811 aerosol size properties from measurements of spectral optical depth using the GRASP algorithm.
812 Atmospheric Measurement Techniques, 10(10), 3743–3781. https://doi.org/10.5194/AMT-10-3743-
813 2017

814   Tsekeri, A., Lopatin, A., Amiridis, V., Marinou, E., Igloffstein, J., Siomos, N., Solomos, S., Kokkalis, P.,
815   Engelmann, R., Baars, H., Gratsea, M., Raptis, P. I., Binietoglou, I., Mihalopoulos, N., Kalivitis, N.,
816   Kouvarakis, G., Bartsotas, N., Kallos, G., Basart, S., … Dubovik, O. (2017). GARRLiC and LIRIC:
817   strengths and limitations for the characterization of dust and marine particles along with their
818   mixtures. Atmospheric Measurement Techniques, 10(12), 4995–5016.
819   https://doi.org/10.5194/AMT-10-4995-2017

820   Walker, J. H., Cromer, C. L., & McLean, J. T. (1991). Calibration of passive remote observing optical
821   and micrwave instrumentation. Proc. SPIE—The International Soc. of Optical Engineering, 3–5
822   April, Orlando, FL, 1493, 224–230.

823   Wei, Y., Li, Z., Zhang, Y., Chen, C., Xie, Y., Lv, Y., & Dubovik, O. (2021). Derivation of PM10 mass
824   concentration from advanced satellite retrieval products based on a semi-empirical physical
825   approach. Remote Sensing of Environment, 256, 112319.
826   https://doi.org/10.1016/J.RSE.2021.112319

827

828   **List of Tables**

829   **Table 1.** Calibration coefficients obtained using simulations of zenith sky radiance (Coef-SIM) and the
830   ones obtained at the IARC against a calibrated integrating sphere (Coef-IARC). The relative difference (Δ)
831   between both coefficients is included assuming Coef-IARC as reference.

λ (nm)	Coef – SIM (W/m²nmsr)	Coef- IARC (W/m²nmsr)	Δ (%)
440	3.2928e-05	3.2485e-05	1.39
500	1.1426e-05	1.2223e-05	-6.54
675	2.0734e-05	2.2221e-05	-6.72
870	1.6840e-05	1.7901e-05	-5.89

832

833   **Table 2.** Determination coefficient (r^2) between ZSR_{ZEN} and ZSR_{PPL} and the mean (MBE), median (Md)
834   and standard deviation (SD) of the Δ differences between ZSR_{ZEN} and ZSR_{PPL} at 440nm, 500nm, 675 nm
835   and 870 nm using the calibration coefficient obtained in this paper with simulated ZSR values and the ones
836   obtained with an integrating sphere at IARC in parenthesis. N represents the number of coincident ZSR_{ZEN}
837   and ZSR_{PPL} data pairs.

	λ (nm)	r^2	MBE (%)	SD (%)	Md (%)	N
	440	0.99 (0.99)	1.96 (0.73)	3.00 (2.95)	1.36 (0.16)	1327
This paper (IARC)	**500**	0.99 (0.99)	-0.34 (6.67)	4.62 (4.95)	-1.39 (5.56)	1317
	675	0.95 (0.95)	3.76 (14.67)	12.54 (13.92)	-0.22 (10.96)	1289
	870	0.94 (0.94)	10.56 (26.67)	21.37 (25.13)	4.99 (20.96)	1165

838
839

840   **List of Figures**
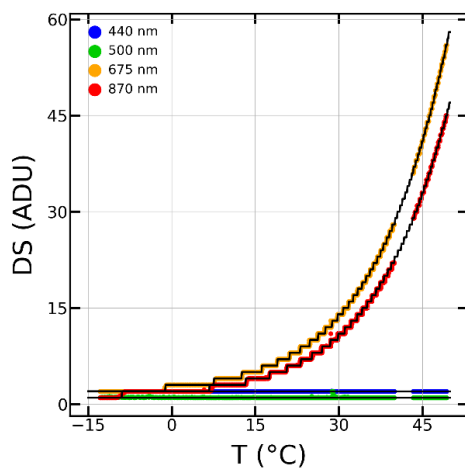
841
842
843 **Figure 1. ZEN-R52 dark signal (DS) in analogic-to-digital units (ADU) against the temperature (coloured dots)**
844 **at 440, 500, 675 and 870 nm. Black lines represent the DS for each channel.**
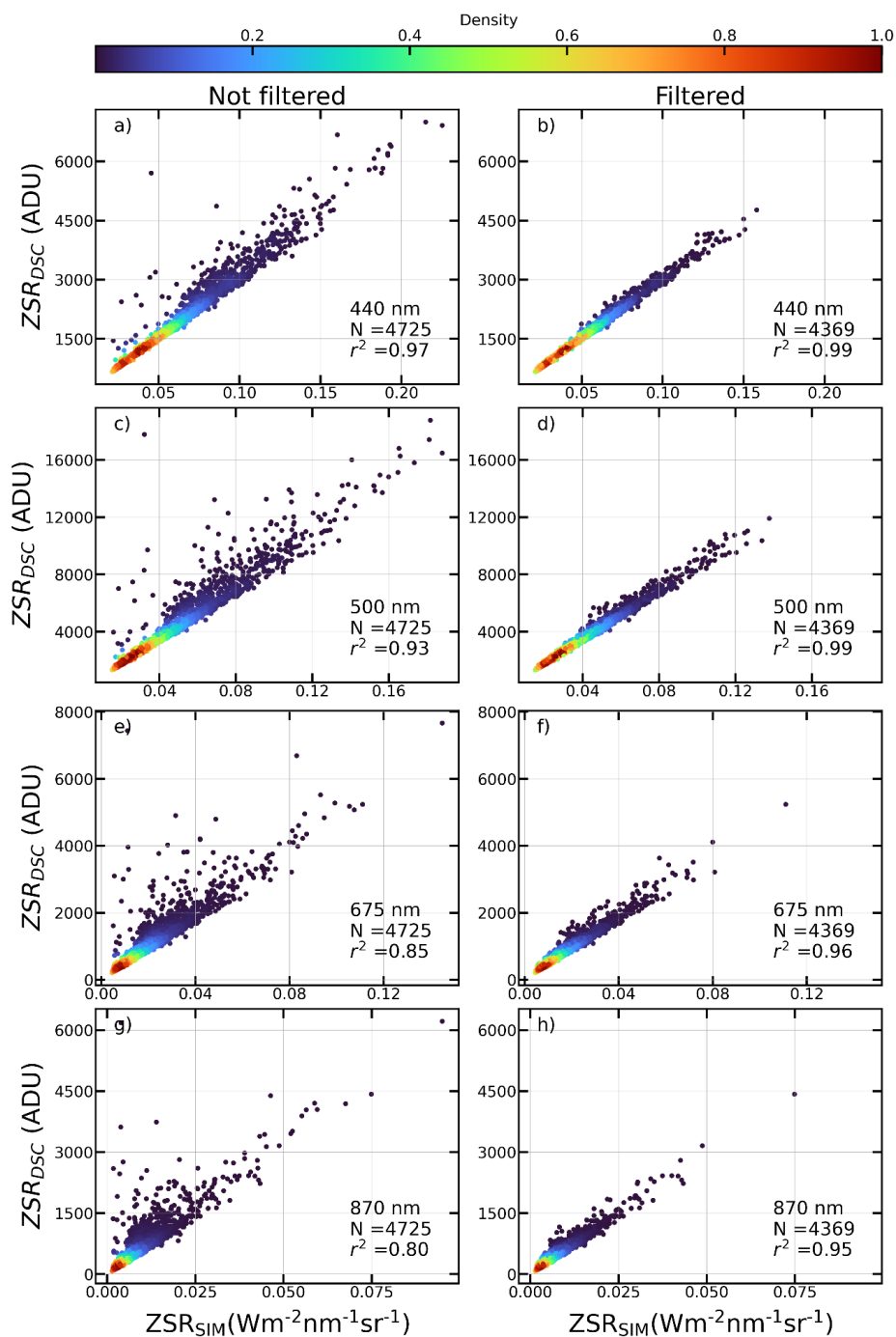
845
846 **Figure 2. Density scatter plot of the measured zenith sky radiances corrected from dark signal (ZSR_{DSC}), in**
847 **analogic-to-digital units (ADU), against the zenith sky radiances simulated by GRASP (ZSR_{SIM}), both at 440 nm**
848 **(upper panels), 500 nm (second row panels), 675 nm (third row panels) and 870 nm (bottom panels). Left and**
849 **right panels show these data before and after applying a quality control filtering, respectively. Determination**
850 **coefficient (r^2) and number of data pairs (N) are also shown.**
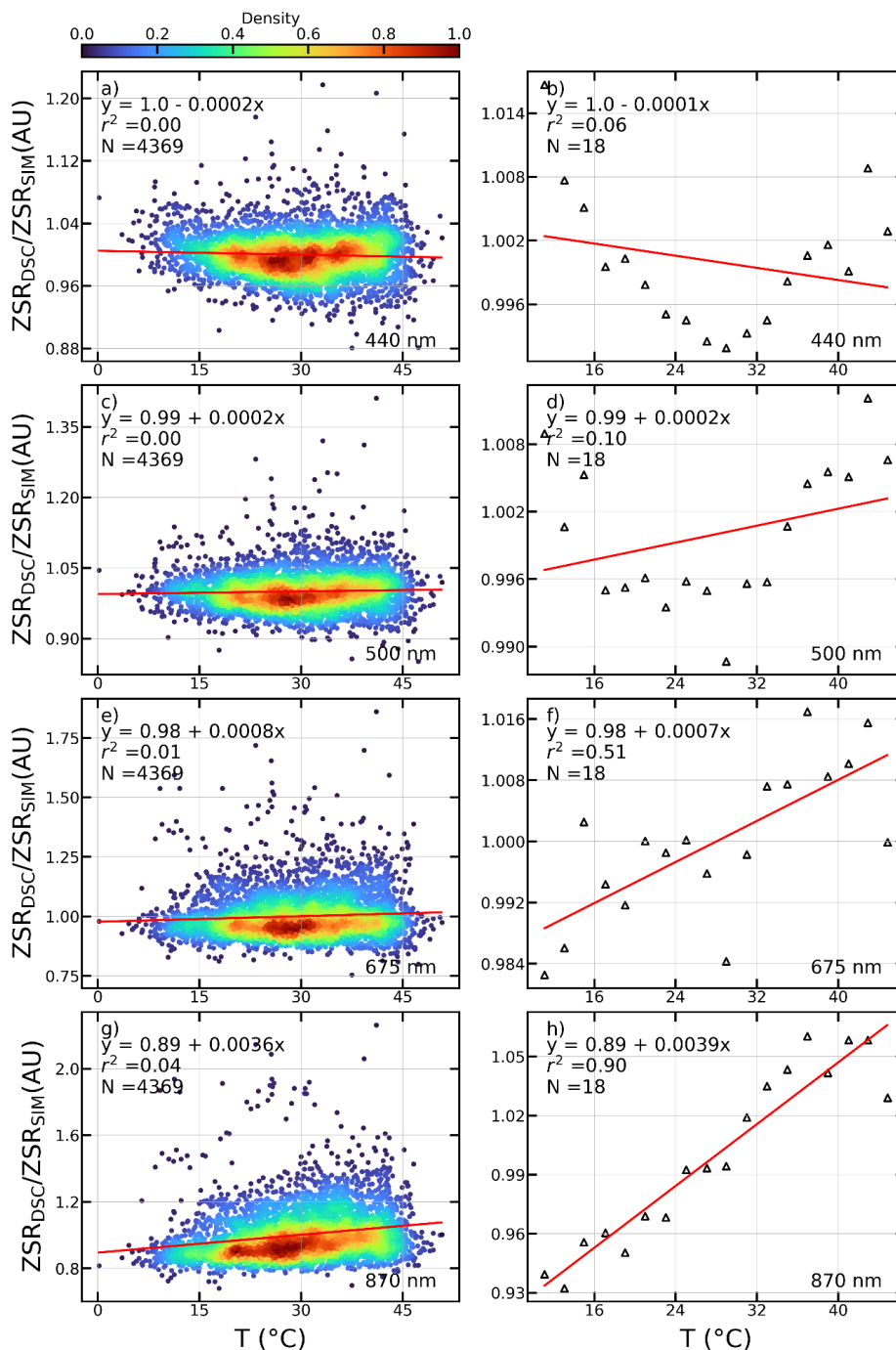
Figure 3. Left panel. density scatter plots for the normalized ratios ZSR$_{DSC}$/ZSR$_{SIM}$ in arbitrary units (AU) against the temperature at a) 440nm, c) 500nm, e) 675 nm and g) 870 nm. Right panel. scatter plot of the median value for the ratios ZSR$_{DSC}$/ZSR$_{SIM}$ grouped in 2°C ranges against mean temperature of the group at b) 440nm,

856   d) 500nm, f) 675 nm and h) 870 nm. Linear fit (red line), determination coefficient (r²) and its equation and
857   number of data points (N) are also shown.

858
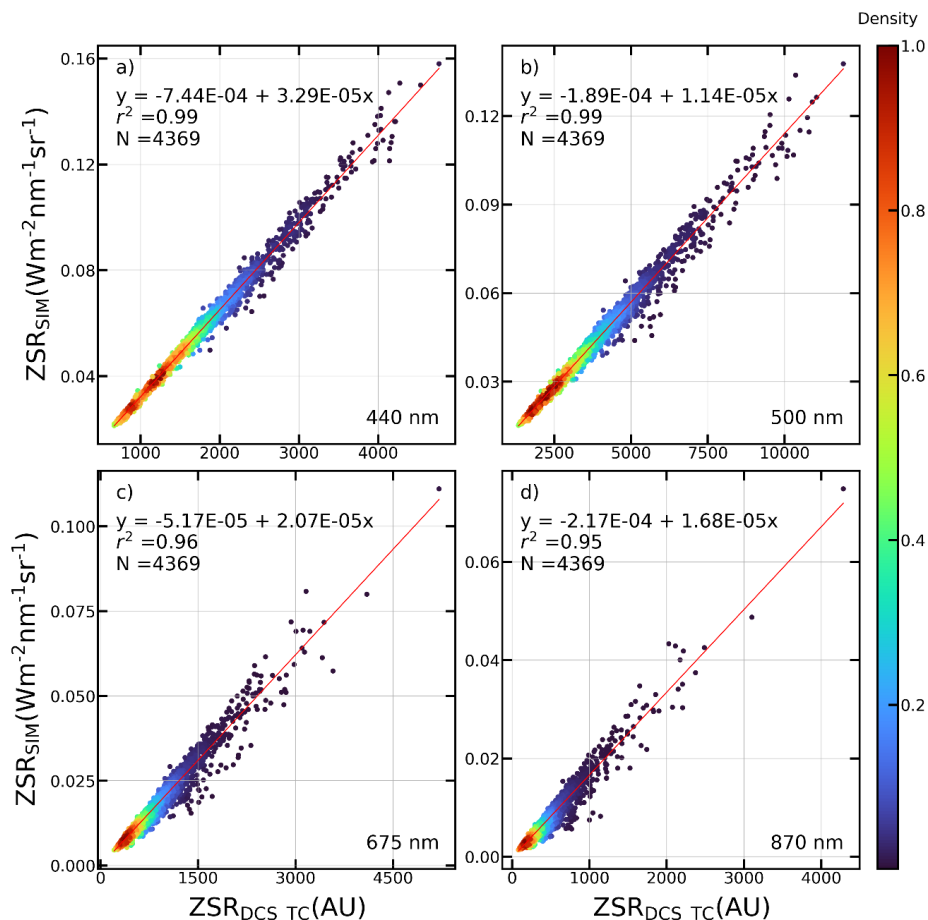
859
860 **Figure 4. Density scatter plot of the zenith sky radiance simulated (ZSR$_{SIM}$) in radiance units against the ZEN-**
861 **R52 measurements in arbitrary units (AU) corrected in dark signal and temperature (ZSR$_{DSC\_TC}$) at a) 440nm,**
862 **b) 500nm, c) 675 nm and d) 870 nm. Linear fit (red line) and its equation, determination coefficient (r²) and**
863 **number of data points (N) are also shown.**
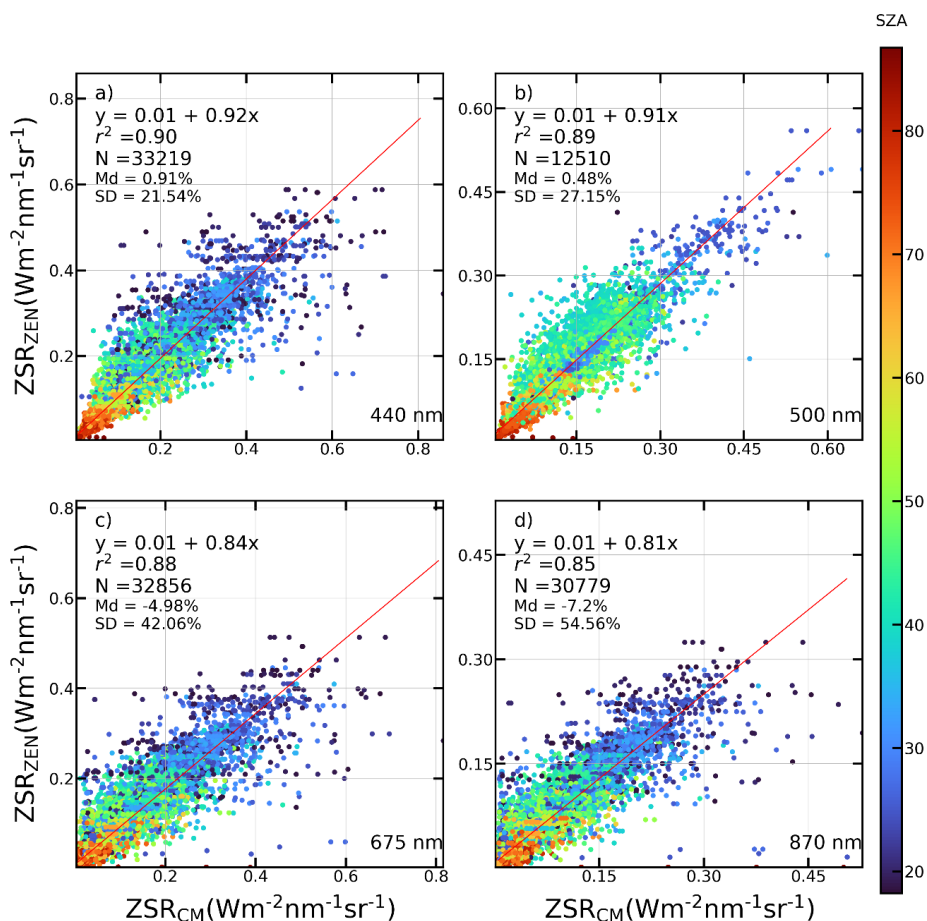
Figure 5. Scatter plot of the calibrated ZEN-R52 measurements (ZSR$_{ZEN}$) against coincident measurements from AERONET Cloud Mode (ZSR$_{CM}$) at a) 440nm, b) 500nm, c) 675 nm and d) 870 nm. Linear fit (red line) and its equation, determination coefficient (r2) and number of data points (N) are shown. The median (Md) and standard deviation (SD) of the Δ differences are also shown. Points colours represent the SZA.
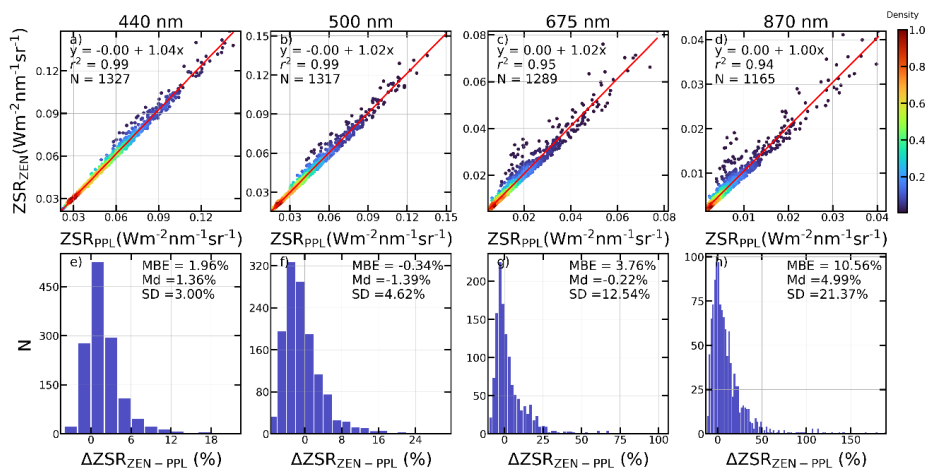
870
871 **Figure 6. (a-d) Density scatter plot of the calibrated ZEN-R52 measurements (ZSR_ZEN) against coincident zenith**
872 **sky radiances derived from AERONET PPL measurements (ZSR_ZEN-PPL) at a) 440 nm, b) 500 nm, c) 675 nm**
873 **and d) 870 nm. Linear fit (red line), its equation, determination coefficient (r²) and number of data pairs (N) are**
874 **shown. (e-h) Frequency histograms of the ΔZSR_ZEN-PPL differences in AOD from ZEN-R52 and AERONET PPL**
875 **e) 440 nm, f) 500 nm, g) 675 nm and h) 870 nm. The mean bias error (MBE), median (Md) and standard**
876 **deviation (SD) of the differences are also shown.**

877

878
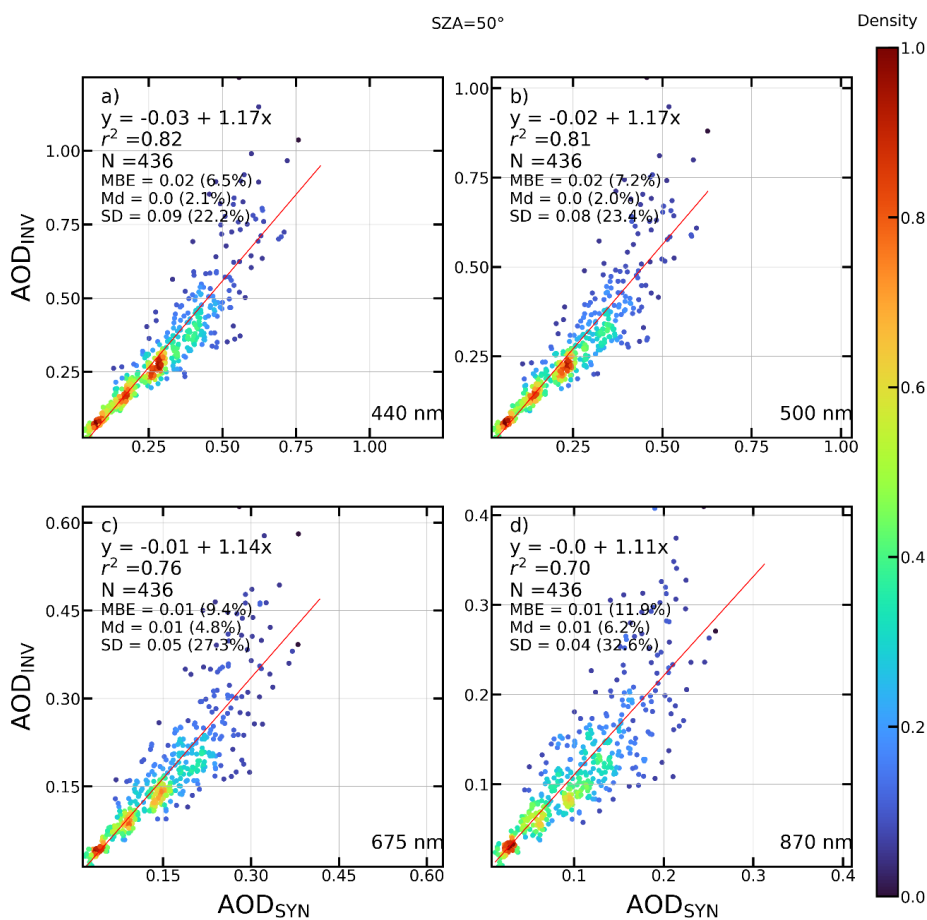
879
880 **Figure 7. Density scatter plot of the AOD retrieved by GRASP after the inversion of synthetic ZSR (AOD_INV)**
881 **against the initial AOD (AOD_SYN) obtained for synthetic scenarios created from the combination of five aerosol**
882 **types for SZA=50° at a) 440nm, b) 500nm, c) 675 nm and d) 870 nm. Linear fit (red line) with its equation,**
883 **determination coefficient (r²) and number of data points (N) are shown. Mean bias error (MB), median (Md)**
884 **and standard deviation (SD) of the absolute and Δ (between brackets) differences between the inverted and**
885 **synthetic AOD are also included.**

Figure 8. Frequency histograms of the absolute differences in the aerosol size distribution properties retrieved by GRASP after the inversion of synthetic ZSR (INV) and the ones initially obtained (SYN) for synthetic scenarios created from the combination of five aerosol types at SZA=50º. The mean bias error (MBE), median (Md) and standard deviation (SD) and their corresponding value for the Δ differences (between brackets) are also shown. These size distribution properties are volume median radius of fine (RF) and coarse (RC) modes, standard deviation of log-normal distribution for fine (σF) and coarse modes (σC), and aerosol volume concentration for fine (VCF) and coarse (VCC) modes and the total (VCT).
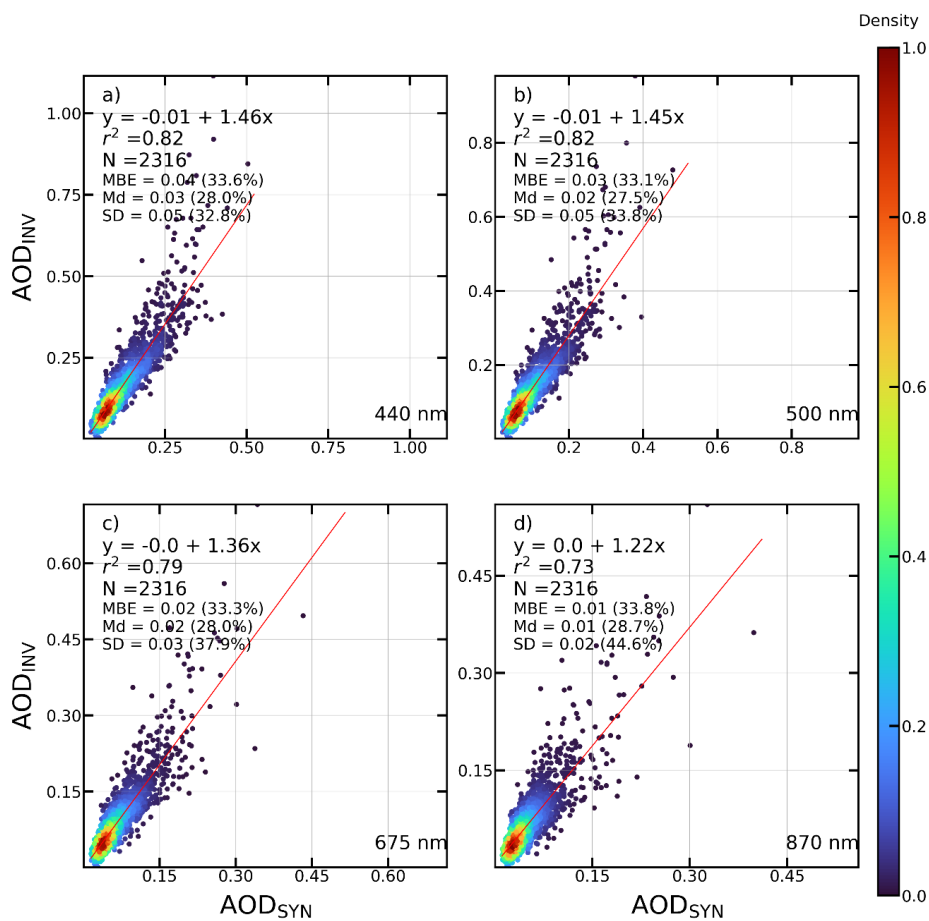
Figure 9. Density scatter plot of the AOD retrieved by GRASP after the inversion of synthetic ZSR (AOD_INV) against the initial AOD (AOD_SYN) obtained for synthetic scenarios created from AERONET retrievals at a) 440nm, b) 500nm, c) 675 nm and d) 870 nm. Linear fit (red line) with its equation, determination coefficient (r^2) and number of data points (N) are shown. Mean bias error (MB), median (Md) and standard deviation (SD) of the absolute and Δ (between brackets) differences between the inverted and synthetic AOD are also included.
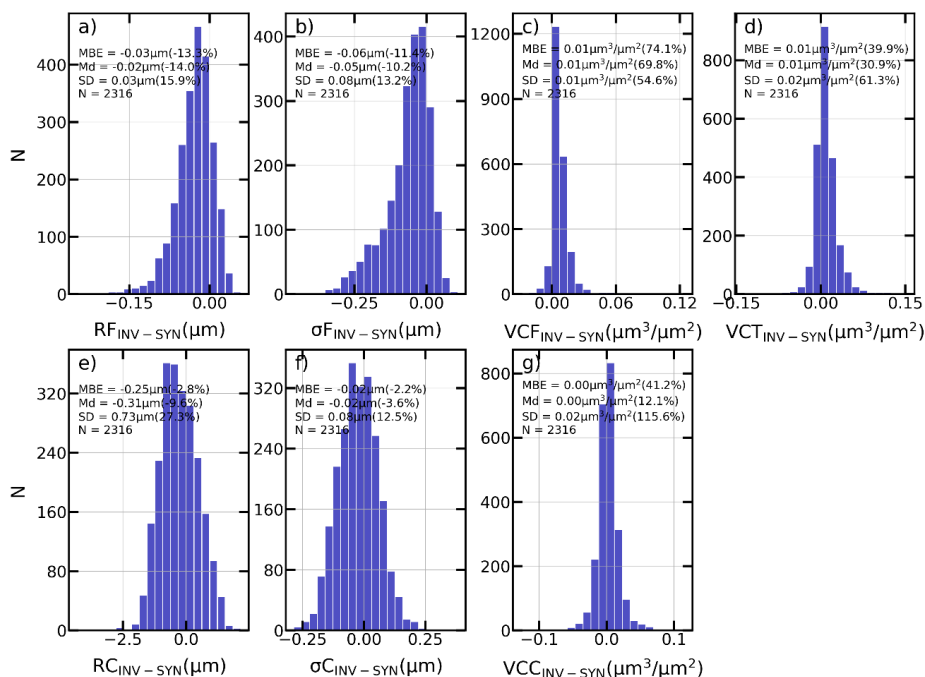
Figure 10. Frequency histograms of the absolute differences in the aerosol size distribution properties retrieved by GRASP after the inversion of synthetic ZSR (INV) and the ones initially obtained (SYN) for synthetic scenarios created from AERONET retrievals. The mean bias error (MBE), median (Md) and standard deviation (SD) and their corresponding value for the Δ differences (between brackets) are also shown. These size distribution properties are volume median radius of fine (RF) and coarse (RC) modes, standard deviation of log-normal distribution for fine (σF) and coarse modes (σC), and aerosol volume concentration for fine (VCF) and coarse (VCC) modes and the total (VCT).
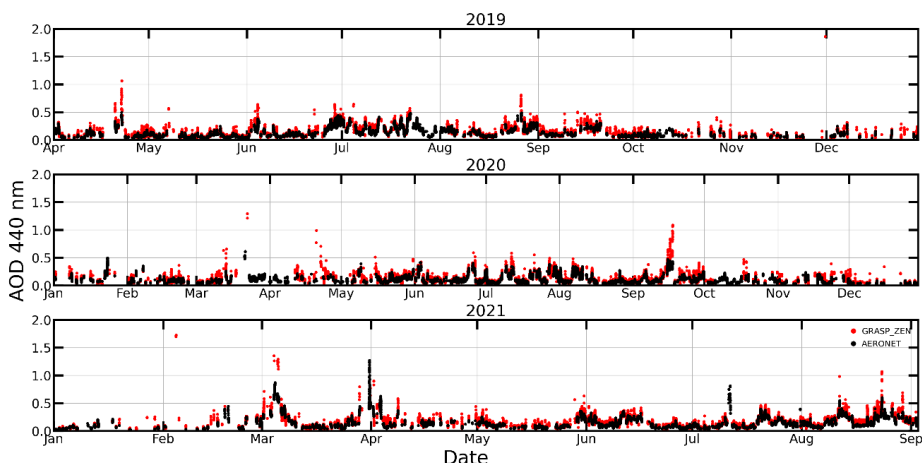
Figure 11. Time series evolution of aerosol optical depth (AOD) at 440 nm retrieved by GRASP-ZEN and by AERONET at Valladolid for all the ZEN-R52 available dataset (April 2019 to September 2021).
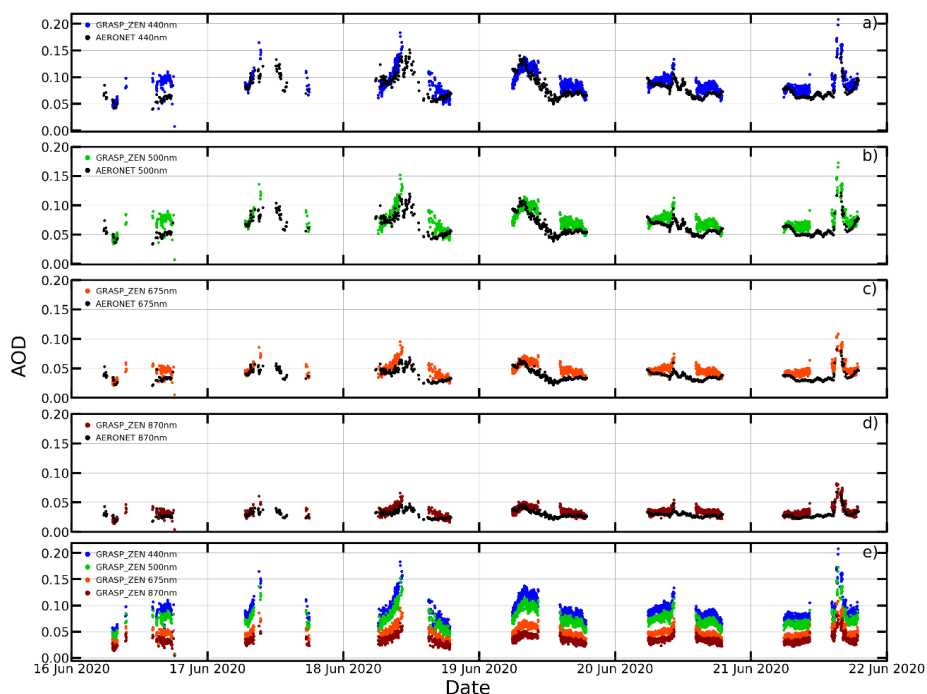
Figure 12. (a-d) Time series evolution of aerosol optical depth (AOD) at a) 440 nm, b) 500 nm, c) 675 nm and d) 870 nm retrieved by GRASP-ZEN and by AERONET at Valladolid for a week period in summer 2020 (16 to 22 June). (e) AOD retrieved by GRASP-ZEN for all ZEN-R52 channels plotted together.
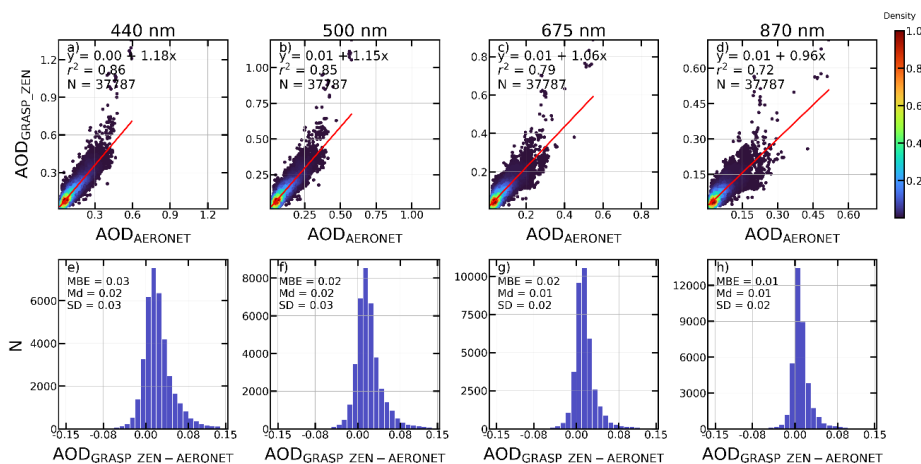
Figure 13. (a-d) Density scatter plots of the AOD retrieved by GRASP-ZEN (AOD$_{GRASP\_ZEN}$) against coincident measurement from AERONET (AOD$_{AERONET}$) at a) 440 nm, b) 500 nm, c) 675 nm and d) 870 nm. Linear fit (red line), its equation, determination coefficient (r^2) and number of data pairs (N) are shown. (e-h) Frequency histograms of the absolute differences in AOD from GRASP-ZEN and AERONET at e) 440nm, f) 500nm, g) 675 nm and h) 870 nm. The mean bias error (MBE), median (Md) and standard deviation (SD) are also shown.
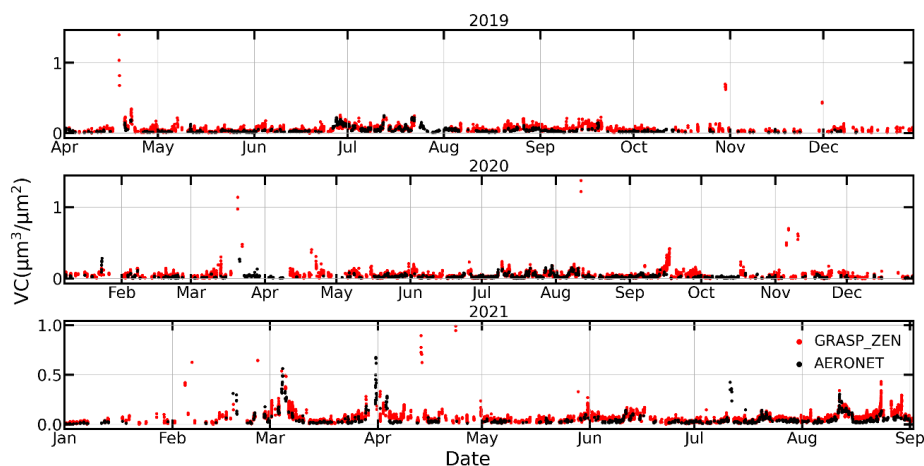
Figure 14. Time series evolution of the total volume concentration (VCT) retrieved by GRASP-ZEN and by AERONET at Valladolid for all the ZEN-R52 available dataset (April 2019 to September 2021).
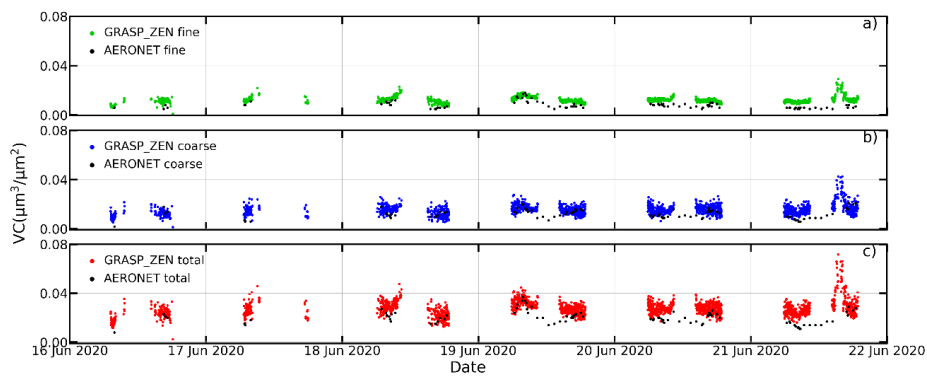
Figure 15. Time series evolution of volume concentration for fine (VCF) and coarse (VCC) modes and the total (VCT) retrieved by GRASP-ZEN and by AERONET at Valladolid for a week period in summer 2020 (16 to 22 June).
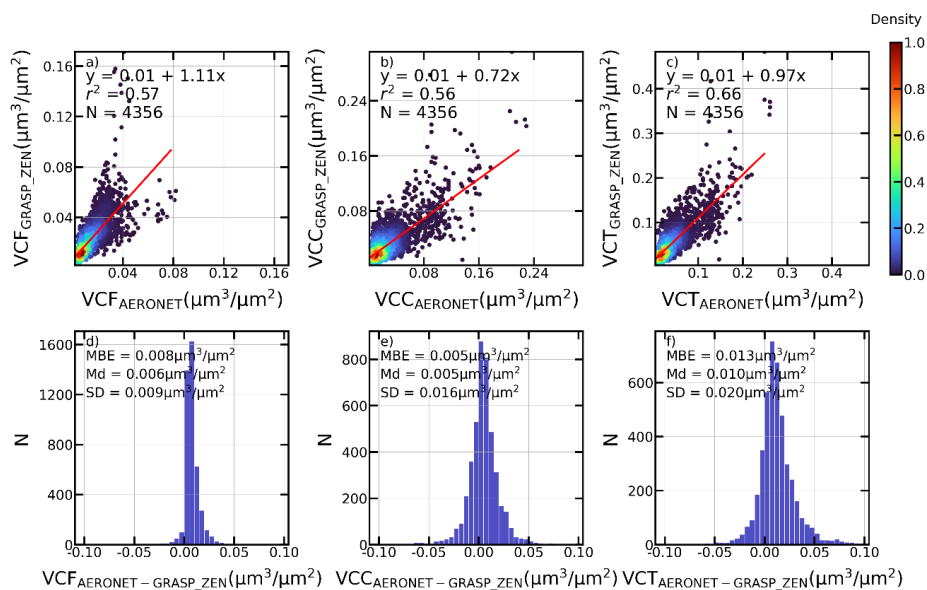
Figure 16. (a-c) Density scatter plot of the volume concentration for fine (VCF) and coarse (VCC) modes and total (VCT) retrieved by GRASP-ZEN against coincident retrievals from AERONET. Linear fit (red line), its equation, determination coefficient (r^2) and number of data points (N) are shown. (e-h) Frequency histograms of the absolute differences between both datasets. The mean bias error (MBE), median (Md) and standard deviation (SD) are also shown.